

UKAEA-CCFE-PR(20)80

O. P. Bardsley, T. C. Hender

On the axisymmetric stability of tokamaks with ferromagnetic walls

Enquiries about copyright and reproduction should in the first instance be addressed to the UKAEA Publications Officer, Culham Science Centre, Building K1/O/83 Abingdon, Oxfordshire, OX14 3DB, UK. The United Kingdom Atomic Energy Authority is the copyright holder.

The contents of this document and all other UKAEA Preprints, Reports and Conference Papers are available to view online free at scientific-publications.ukaea.uk/

On the axisymmetric stability of tokamaks with ferromagnetic walls

O. P. Bardsley, T. C. Hender

On the axisymmetric stability of tokamaks with ferromagnetic walls

O.P. Bardsley, T.C. Hender

May 27, 2020

Abstract

Reduced activation ferritic steels are an attractive option for use in large structural components surrounding tokamak plasmas in future fusion power plants, but their ferromagnetic response to the confining magnetic fields must be properly understood. Simultaneously, the advantages of operating at high plasma elongation push tokamak designs toward scenarios which are more vulnerable to vertical displacement events. Passive conducting structures in present tokamaks slow these instabilities such that they may be feedback controlled, but the efficacy of this process is likely to be eroded by ferromagnetic effects. We approach two related analytical models – in cylindrical and spherical geometries – which qualitatively and quantitatively assess the impact of a ferritic steel wall on the vertical instability growth rate for a plasma of certain elongation. Distinct limits for magnetically thick and thin walls give key physical insight, but the dependence on magnetic permeability and wall geometry is in general quite complex. Equilibrium considerations, particularly with respect to radial force balance, are also encountered.

1 Introduction

The first generation of nuclear fusion power plants will have to be built from materials capable of operating reliably when subjected to high fluences of 14MeV neutrons. In particular, structural steels surrounding a burning tokamak plasma must be robust to both displacement damage and radioactivation, in order to achieve sufficient operational availability and simplify the decommissioning process [1]. At present, the leading candidate materials for applications in the first wall and tritium breeding modules are reduced activation ferritic-martensitic (RAFM) steels [2, 3] such as EUROFER-97 [4]; unlike the stainless steels widely used in current tokamak experiments, these are ferromagnetic and as such have an effect on the confining magnetic field which is more complex than just the electromagnetic induction of eddy currents. Ferromagnetism will alter both the equilibrium arrangement of flux surfaces – and in fact is used as a means of reducing toroidal field ripple [5, 6] – and the time-dependent response of the vessel to changes in the plasma position or current.

At the same time, it is known to be advantageous for tokamak performance to operate at large values of plasma elongation, defined as the ratio of vertical to horizontal extents of its cross-section [7]. Increasing elongation beyond the value it would naturally take in a uniform vertical field leads to axisymmetric instability; such vertical displacement events (VDEs), which would proceed at the Alfvén velocity in the absence of a vessel, are slowed to ‘resistive wall’ timescales by the presence of surrounding conductors, to such a point they may be tamed by an active feedback control system.

Vertical stability is an important issue in tokamak reactor design; reliable plasma positioning is important for moderating divertor heat loads [8], but at worst VDEs involving high-energy plasmas can lead to extreme

heat loads and electromagnetic forces upon impact with the vessel wall which will be intolerable in reactor-scale tokamaks [9]. Hence, there is a vital need to understand changes to the plasma's vertical stability characteristics when significant quantities of the material surrounding the plasma is exchanged for a ferromagnetic equivalent. It is this need which motivates the present study, which encompasses two closely-related analytical model problems — one in an infinite aspect ratio (i.e. cylindrical) geometry, section 2, and one in a spherical geometry, section 3. We bookend these with a short introduction to ferromagnetism in tokamaks (section 1.1) and a discussion of possible implications for the design of future devices with opportunities for further study (section 4).

1.1 Ferromagnetic materials in tokamaks

Ferromagnetic materials are distinguished by a constitutive relation between the magnetic field \mathbf{H} and magnetic flux density \mathbf{B} within their volume which differs dramatically from that for conventional materials, $\mathbf{B} = \mu_0 \mathbf{H}$, where μ_0 is the magnetic permeability of free space. The permeability of a ferromagnet is much larger at small \mathbf{H} but saturates at large applied fields; in a tokamak, the dominant toroidal field can be expected to drive the material deep into saturation (the saturating magnetic field is $\mu_0 H_s \sim 0.25\text{T}$ for EUROFER-97 [4]). The effective magnetic permeability as experienced by the poloidal magnetic field, μ_1 , then depends upon the saturation magnetisation of the material M_s and the applied toroidal magnetic field H_ϕ ,

$$\frac{\mu_1}{\mu_0} \equiv \tilde{\mu} \approx 1 + \frac{M_s}{H_\phi}, \quad (1)$$

if the poloidal field strength is significantly weaker than the toroidal. This expression defines the *effective relative magnetic permeability* $\tilde{\mu}$; for EUROFER-97, the saturation magnetisation is $\mu_0 M_s \sim 1.8\text{T}$ [4], so a toroidal field of a couple of Tesla amounts to $\tilde{\mu} \sim 2$, with larger values for weaker fields.

Note that the boundary conditions across an interface between a vacuum and a ferromagnetic wall depend on the effective magnetic permeability of the material in question; in particular, normal magnetic *flux* and tangential magnetic *field* must both be conserved [10]:

$$\langle \mathbf{B} \cdot \mathbf{n} \rangle = \left\langle \frac{\mathbf{B} \times \mathbf{n}}{\mu} \right\rangle = 0, \quad (2)$$

where \mathbf{n} is the normal to the interface, μ ($= \mu_0$ or μ_1) is the effective magnetic permeability in each domain, and the angled brackets represent the jump across the boundary.

2 Large aspect ratio tokamaks: a cylindrical model problem

We first consider a model problem in the large aspect ratio cylindrical limit, similar to that of used for previous studies of ferromagnetic resistive wall modes (FRWMs) [11]. The layout is sketched in figure 1; the ferromagnetic, conducting wall is taken to be a continuous cylindrical shell of internal radius r_i and external radius r_e . It has an electrical conductivity σ and permeability μ_1 , both of which are taken to be constant throughout its volume. The rest of the domain is vacuum with magnetic permeability μ_0 . Polar co-ordinates (r, θ) , as indicated in figure 1, are the natural choice in this geometry, and all quantities are assumed independent of distance along the cylinder. The plasma is represented by a thin wire carrying a constant current I_p , directed into the page and located a small distance z_p above the origin; in equilibrium, the plasma height will be zero, but during a VDE will grow exponentially in time. The divertor coils, which act to elongate the plasma, are represented by thin wires placed exterior to the wall at $r = r_c$, directly above and below the plasma at $\theta = [0, \pi]$, which each carry a constant current I_c in the same direction as the plasma current. Increasing the divertor current I_c relative to the plasma current I_p will increase the vertically destabilising force on the plasma, and thereby increase the

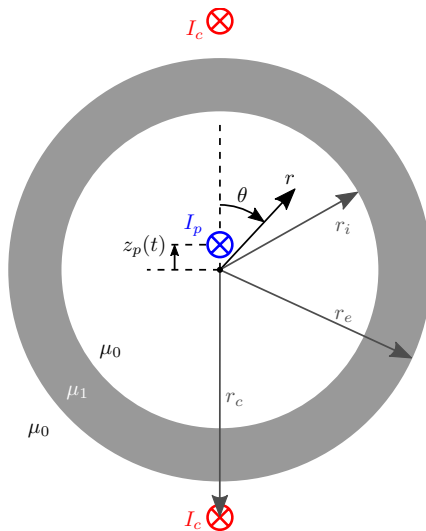


Figure 1: Schematic of the cylindrical model problem, showing geometry, parameters and co-ordinates.

instability growth rate. Note that, in this infinite aspect ratio case, no vertical field need be applied in order to maintain horizontal force balance.

As the magnetic flux density is two-dimensional and divergence-free, it may be written using a flux function $\psi(r, \theta, t)$:

$$\mathbf{B} = \nabla\psi \times \mathbf{e}_{\parallel} = \frac{1}{r} \frac{\partial\psi}{\partial\theta} \mathbf{e}_r - \frac{\partial\psi}{\partial r} \mathbf{e}_{\theta} \quad (3)$$

where \mathbf{e}_{\parallel} , \mathbf{e}_r and \mathbf{e}_{θ} are the unit vectors in the directions of positive I_p , increasing r , and increasing θ respectively. The boundary conditions (2) across the wall-vacuum interfaces r_i and r_e then become

$$\left\langle \frac{\partial\psi}{\partial\theta} \right\rangle = \left\langle \frac{1}{\mu} \frac{\partial\psi}{\partial r} \right\rangle = 0. \quad (4)$$

We identify three separate solution regions: interior to the wall ‘(i)’, within the thickness of the wall itself ‘(w)’, and exterior to the wall ‘(e)’. General solutions for the magnetic flux in each region will be matched via the boundary conditions (4).

2.1 Equilibrium solution

First, we derive the equilibrium solution when the plasma is stationary, which has a flux function $\Psi(r, \theta)$. Since there is no motion, no current flows in the wall and the flux function satisfies $\nabla^2\Psi = 0$ everywhere. The solution then consists of two distinct portions – the magnetic flux due to the plasma wire, and that due to the divertor coils – which we approach sequentially.

2.1.1 Plasma wire

We begin with the magnetic flux due to the plasma wire in equilibrium at an arbitrary height z_p , denoted by a superscript ‘(p)’. Note that, in the vertical stability problem, the plasma is never held stationary at a finite height by definition, and so the solution with non-zero z_p is inherently unsteady. Nevertheless, the steady field due to a plasma wire at an arbitrary height will prove useful in the following discussion, and so is presented below.

First, observe that in the absence of any ferromagnetic effect, the solution can be expressed as the series

$$\Psi^{(p)} = \frac{\mu_0 I_p}{2\pi} \left(-\ln r_{>} + \sum_{m=1}^{\infty} \left(\frac{r_{<}}{r_{>}} \right)^m \frac{\cos m\theta}{m} \right), \quad (5)$$

where r_{\leq} is the lesser/greater of r and z_p . In the presence of the ferromagnetic wall, since $\Psi^{(p)}$ is still a harmonic function the general form of the solution is

$$\Psi^{(p)} = \sum_{m=0}^{\infty} \hat{\Psi}_m^{(p)}(r) \cos m\theta \quad (6)$$

where

$$\hat{\Psi}_0^{(p)} = -\frac{\mu_0 I_p}{2\pi} \times \begin{cases} \ln r > & (i) \\ \tilde{\mu} \ln r - (\tilde{\mu} - 1) \ln r_i & (w) \\ \ln r - (\tilde{\mu} - 1) \ln(r_i/r_e) & (e) \end{cases} \quad (7)$$

$$\hat{\Psi}_{m \geq 1}^{(p)} = C_m^{(p)} \left(\frac{r_i}{r}\right)^m + D_m^{(p)} \left(\frac{r}{r_i}\right)^m, \quad (8)$$

and the coefficients $C_m^{(p)}$, $D_m^{(p)}$ take on different values in the three regions ($i/w/e$). The boundary conditions (4) have already been applied to the $m = 0$ term, but we now approach them for the $m \geq 1$ coefficients. By comparison with (5), the known internal ‘source’ coefficients due to the plasma wire are

$$C_m^{(p,i)} = \frac{\mu_0 I_p}{2\pi m} \left(\frac{z_p}{r_i}\right)^m. \quad (9)$$

Furthermore, as there are no sources outside of the wall (divertor coils being ignored for now) we must have $D_m^{(p,e)} = 0$. The four boundary conditions (4) applied to (8) thus give a set of simultaneous equations for the remaining coefficients $D_m^{(p,i)}$, $C_m^{(p,w)}$, $D_m^{(p,w)}$ and $C_m^{(p,e)}$, solved in appendix A.1. Of particular interest here is the horizontal magnetic flux density at the origin due to the magnetism of the wall, since it will be proportional to the (destabilising) vertical Lorentz force exerted on the plasma for small displacements z_p . We denote this $B_R^{(p)}$, in analogy with the major radial co-ordinate R in a toroidal tokamak geometry, and define it as positive when pointing to the right in figure 1. It is

$$B_R^{(p)} \approx \frac{-D_1^{(p,i)}}{r_i} = \frac{-\mu_0 I_p z_p}{2\pi r_i^2} \frac{(r_i/r_e) - (r_e/r_i)}{\frac{\tilde{\mu}-1}{\tilde{\mu}+1} (r_i/r_e) - \frac{\tilde{\mu}+1}{\tilde{\mu}-1} (r_e/r_i)}. \quad (10)$$

If the wall is thin in a geometrical sense, $\delta_w = r_e - r_i \ll r_i$, then this simplifies to

$$B_R^{(p)} \approx \frac{-\mu_0 I_p z_p \delta_w}{4\pi r_i^3} \left(\tilde{\mu} - \frac{1}{\tilde{\mu}}\right). \quad (11)$$

As one might expect, increasing either the wall thickness or the effective magnetic permeability increases the ferromagnetic force which acts on the plasma. It is important to reiterate that these expressions are only valid for a *stationary* plasma wire, and therefore represent the destabilising ferromagnetic force which would act in the limit of a slow-growing instability – in the sense that the growth time is much greater than the resistive wall time – during which the magnetic flux within the wall has time to reconfigure itself and remain close to its quasi-steady value.

2.1.2 Divertor coils

The other half of the solution is that due to the divertor coils placed above and below the plasma, and exterior to the wall, denoted by the superscript ‘(c)’. The mathematics is much the same as the previous section, with a few minor alterations. First, owing to the additional symmetry only even- m terms contribute, and furthermore the $m = 0$ term is unaltered by the presence of the wall, $\hat{\Psi}_0^{(c)} = -(\mu_0 I_c/\pi) \ln r_{>}$. Second, r_{\leq} is now the lesser/greater of r and r_c . Third, the current is now external to the wall so the known coefficients are

$$D_m^{(c,e)} = \frac{\mu_0 I_c}{\pi m} \left(\frac{r_i}{r_c}\right)^m \quad (12)$$

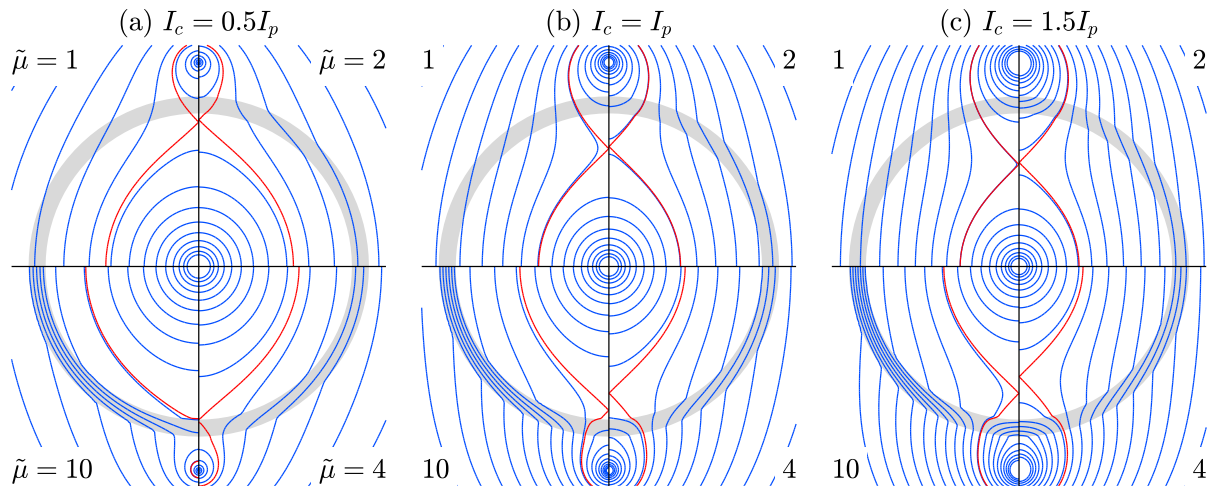


Figure 2: Example equilibrium configurations in the cylindrical problem with a ferromagnetic wall ($r_i = 0.9r_e$, grey shading) and divertor coils ($r_c = 1.2r_e$). The divertor current I_c varies between the panes and the effective relative permeability $\tilde{\mu}$ varies between the quadrants, increasing clockwise from top-left. Flux surfaces (at the same levels in all plots) are shown in blue, and the LCFS in red.

and the $C_m^{(c,i)}$ must be zero in order to ensure regularity at the origin. We may again solve for a solution of the form (8) using the boundary conditions (4) — see appendix A.2. The salient result is the vertical gradient of the horizontal magnetic flux density at the origin — although $B_R^{(c)}$ is zero at the origin itself, at a small height z_p above it we have

$$B_R^{(c)} = \frac{-2z_p D_2^{(c,i)}}{r_i^2} = \frac{-\mu_0 I_c z_p}{\pi r_c^2} \frac{4\tilde{\mu}}{(\tilde{\mu} + 1)^2 - (\tilde{\mu} - 1)^2 (r_i/r_e)^4}. \quad (13)$$

This is proportional to the destabilising force gradient acting on the plasma wire due to the presence of the divertor coils. In the limit of a geometrically thin wall, this becomes

$$B_R^{(c)} \approx \frac{-\mu_0 I_c z_p}{\pi r_c^2} \left(1 - \frac{(\tilde{\mu} - 1)^2}{\tilde{\mu}} \frac{\delta_w}{r_i} \right) \quad (14)$$

which makes it clear that increasing the magnetic permeability reduces the destabilising force gradient due to the external coils, by virtue of the magnetic shielding effect.

2.1.3 Ferromagnetic effects on the equilibrium

Quite clearly, the presence of the ferromagnetic wall has an effect on the equilibrium magnetic flux distribution. Figure 2 shows some simple equilibria with a plasma wire at the origin and a divertor coil pair carrying various currents I_c . Within each pane, four different equilibria are plotted, for $\tilde{\mu} = [1, 2, 4, 10]$, one in each quadrant. Notice how, as the magnetic permeability is increased, the flux surfaces are increasingly channelled through the wall, reducing their penetration into the interior and allowing expansion of the internal flux surfaces.

To describe the shape of the interior magnetic flux, we introduce the plasma elongation κ , defined as the ratio of vertical to horizontal extents of the last closed flux surface (LCFS), which is itself determined either by the location of an internal null (‘X-point’), or the wall inner radius (‘limited’), whichever is closer to the origin. The LCFS is shown as red lines in figure 2. Note that, since no attempt is made to treat a distributed plasma current or pressure, this definition of κ is only a proxy for the true plasma elongation, which will depend on the plasma’s internal inductance in addition to the externally-applied field.

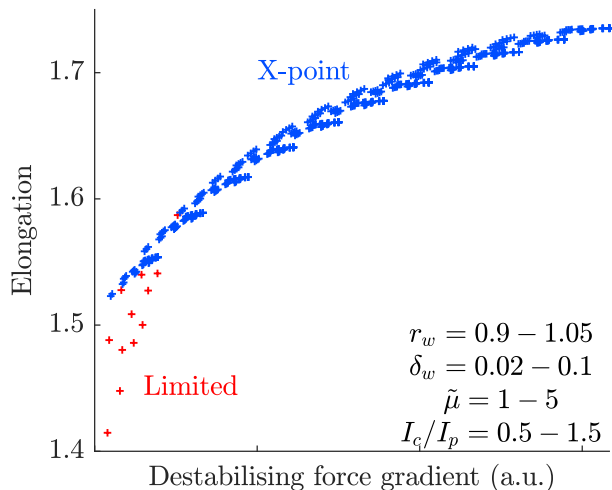


Figure 3: Elongation of the last closed flux surface as a function of the destabilising force gradient due to divertor coils (13) for a scan of wall location, wall thickness, magnetic permeability, and divertor current over the ranges indicated. The divertor coils are at $r_c = 1.2$. Wall-limited cases are shown in red and X-point cases in blue.

The equilibrium quantity of most interest to us is the destabilising force gradient due to the external coils, given in (13). It is well known [12, 13] that in the absence of any ferromagnetic effect this quantity is strongly related to the plasma elongation; we now show that this is still the case in the presence of a ferromagnetic wall. Figure 3 shows plasma elongation as a function of the destabilising force gradient ($\propto -dB_R^{(e)}/dz_p$, see (13)) across a range of parameter values — wall location $r_w = (r_i + r_e)/2$, wall thickness, relative permeability, and divertor current are all varied simultaneously. For the X-point configurations, there is a strong correlation between elongation and the destabilising force gradient, implying that, once the plasma elongation has been specified as a design constraint, so too has the destabilising force gradient due to the external coils, independent of the existence of any ferromagnetic effect. A larger $\tilde{\mu}$ simply increases the external currents required in order to achieve that elongation, in accordance with (13) or (14). Note, however, that this says nothing about the destabilising ferromagnetic force (10), which has no such connection to the plasma elongation and increases with $\tilde{\mu}$.

2.2 Time-dependent solution

We now move our discussion to the time-dependent field due to currents induced in the wall when the plasma is displaced vertically with an instability growth rate γ , that is $z_p \propto e^{\gamma t}$. In the non-ferromagnetic situation, this force is always stabilising, and the induced currents in the wall act to slow down the instability. When the wall is ferromagnetic, however, these currents must compete with the destabilising force due to the magnetic attraction between plasma and wall, as derived in section 2.1.1, equation (10). Hence it is not immediately obvious whether the wall will provide a net stabilising or destabilising influence when ferromagnetic effects are taken into account.

We proceed to calculate the unsteady flux function $\psi(r, \theta, t)$, which is governed by a diffusion equation within the conducting wall, but still satisfies Laplace's equation in the vacuum regions:

$$\mu_1 \sigma \frac{\partial \psi}{\partial t} = \nabla^2 \psi \quad (w) \quad (15)$$

$$0 = \nabla^2 \psi \quad (i, e). \quad (16)$$

In the limit of small plasma displacement, the general solution to leading order in z_p may be written as

$$\psi = \hat{\psi}(r)e^{\gamma t} \cos \theta \quad (17)$$

where

$$\hat{\psi}(r)e^{\gamma t} = \begin{cases} c^{(i)} \left(\frac{r_i r_{\leq}}{z_p r_{>}} \right) + d^{(i)} \left(\frac{r}{r_i} \right) & (i) \\ c^{(w)} I_1(y) + d^{(w)} K_1(y) & (w) \\ c^{(e)} \left(\frac{r_i}{r} \right) & (e). \end{cases} \quad (18)$$

Here, r_{\leq} is the lesser/greater of r and z_p , with $I_1(y)$ and $K_1(y)$ the modified Bessel functions of order 1 and argument $y = r\sqrt{\mu_1\sigma\gamma}$. Lower case is used for the coefficients $c^{(\cdot)}$ and $d^{(\cdot)}$ to emphasise they are part of the time-dependent solution; by comparison with (9) we can see that $c^{(i)} = \mu_0 I_p z_p / 2\pi r_i$ is known but the remaining coefficients must be determined from the boundary conditions (4). (Note that $d^{(e)} = 0$ to ensure regularity as $r \rightarrow \infty$.) This is done in appendix A.3; the resulting horizontal magnetic flux at the origin, tantamount to the unsteady Lorentz force exerted on the plasma, is

$$b_R = -\frac{\mu_0 I_p z_p}{2\pi r_i^2} \frac{d^{(i)}}{c^{(i)}} \quad (19)$$

with $d^{(i)}/c^{(i)}$ from (71). For a given geometry the reactive force acting back on the plasma due to the wall depends in a non-trivial way upon the instability growth rate γ and the wall's effective magnetic permeability μ_1 ; this is shown by the solid lines in figure 4. As the growth rate (which is normalised to the non-ferromagnetic wall time $\tau_{w0} = \mu_0\sigma\delta_w^2$) increases, so too does the stabilising wall force as a result of the larger currents induced within the wall. If the wall is ferromagnetic, this force is decreased with respect to the $\tilde{\mu} = 1$ case, such that it even becomes negative (i.e. destabilising rather than stabilising) at smaller values of γ — this emulates previous studies into the dependence of FRWMs on rotation frequency [14, 15]. The asymptote as $\gamma\tau_{w0} \rightarrow 0$ is shown by the horizontal dotted lines, calculated using the solution (10) for a plasma wire held stationary at a height z_p . Hence, if the instability growth rate is slow compared to the wall time, such that the internal magnetic flux evolves in a quasi-steady manner, then the effect of ferromagnetism is to provide an additional destabilising force, one which is not associated with the equilibrium magnetic flux configuration and therefore does not come with the dividend of an increase in plasma elongation.

If the instability growth rate is large compared to the wall time, however, the story is somewhat different. In this case the magnetic skin depth $s \sim (\mu_1\sigma\gamma)^{-1/2}$ is much less than the wall thickness and so the choice of r_e is in practice irrelevant. Regularity at infinity then demands $c^{(w)} = 0$ and so the expression for b_R simplifies to

$$b_R \approx \frac{\mu_0 I_p z_p}{2\pi r_i^2} \frac{y_i K_0(y_i) - (\tilde{\mu} - 1)K_1(y_i)}{y_i K_0(y_i) + (\tilde{\mu} + 1)K_1(y_i)} \approx \frac{\mu_0 I_p z_p}{2\pi r_i^2} \left(1 - \frac{2\tilde{\mu}}{y_i} + \mathcal{O}(y_i^{-2}) \right), \quad (20)$$

where the latter form is the limit as $y_i \rightarrow \infty$ ($s \ll r_i$). This is plotted as dashed lines in figure 4. It is important to notice that the expression above depends on γ and $\tilde{\mu}$ only through the term

$$\frac{y_i}{\tilde{\mu}} = r_i \sqrt{\frac{\mu_0\sigma\gamma}{\tilde{\mu}}}, \quad (21)$$

and so they only enter the stabilising force in the combination $\gamma/\tilde{\mu}$. This suggests that, for a given destabilising force gradient, growth rates will be larger by a factor $\tilde{\mu}$ for ferromagnetic cases in which the wall may be considered magnetically thick; this is also concluded in studies of FRWMs using a similar model [11].

Note that, regardless of the value of $\tilde{\mu}$, there is maximum possible b_R equal to the ideal-wall value $b_{R,max} = \mu_0 I_p z_p / 2\pi r_i^2$, reached in the limit of infinite growth rate. This means that if the magnitude of the destabilising force due to external coils ($B_R^{(c)}$, equation 13) is greater than $b_{R,max}$ then the conducting wall alone is insufficient to slow the instability to sub-Alfvénic speeds, meaning the equilibrium is ideally unstable.

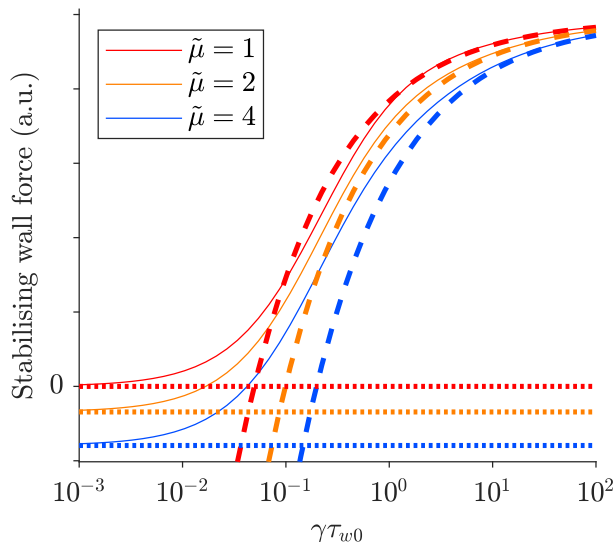


Figure 4: Force due to the wall as a function of the instability growth rate for different $\tilde{\mu}$. The geometry is as figure 3, $r_i = 0.9r_e$. Dashed lines show the ‘thick-wall’ (large γ) limit given by (20) and dotted lines the ‘thin-wall’ (small γ) limit given by (10).

2.3 Calculation of growth rate

Having now derived both the equilibrium and time-dependent Lorentz forces acting on the plasma wire, we proceed to calculate the instability growth rate γ as a function of the problem parameters. We consider a plasma of negligible mass whose vertical position increases exponentially, but nevertheless always remains close to the origin such that the problem may be linearised. Since the plasma is massless, the total vertical Lorentz force at its location must be zero, or equivalently

$$B_R^{(c)} + b_R = 0 \quad (22)$$

where $B_R^{(c)}$ comes from (13) and b_R from (19). This constitutes an equation for the growth rate γ which may be easily solved numerically; example curves of growth rate versus the destabilising force gradient are given in figure 5. As suggested by the discussion of the previous section, there is a dichotomy between fast- and slow-growing instabilities, and so we treat the two extremes separately below.

2.3.1 Fast (thick wall) instability

The ‘fast’ limit of (22) is characterised by a magnetic skin depth which is much less than the thickness of the wall ($s \ll \delta_w$), or equivalently a growth rate much greater than the resistive wall time ($\gamma\tau_{w0} \gg 1$). Because the skin effect predominates, the internal magnetic flux is relatively slow to react to the motion of the plasma wire, and the destabilising ferromagnetic effect of the *equilibrium* solution in section 2.1.1 is not felt by the plasma. Hence the destabilising influence is purely due to the existence of the divertor coils, and the impact of ferromagnetism is solely a reduction in the magnitude of the stabilising wall force (19). In particular, b_R is given by the limiting form (20) which, as discussed there, is a function of γ and $\tilde{\mu}$ only in the combination $\gamma/\tilde{\mu}$. The external destabilising force $B_R^{(c)}$ (equation 13), despite ostensibly depending on the magnetic permeability, is fixed by the plasma elongation as discussed in section 2.1.3. Hence, for a given elongation, growth rates are inflated by a factor $\tilde{\mu}$ relative to the non-ferromagnetic case in situations where the wall is thicker than the magnetic skin depth; this is evidenced in figure 5(a), which shows a coalescence of the curves of $\gamma/\tilde{\mu}$ versus $B_R^{(c)}$ for $\gamma\tau_{w0} \gtrsim 1$, as they asymptote towards the ideal stability limit.

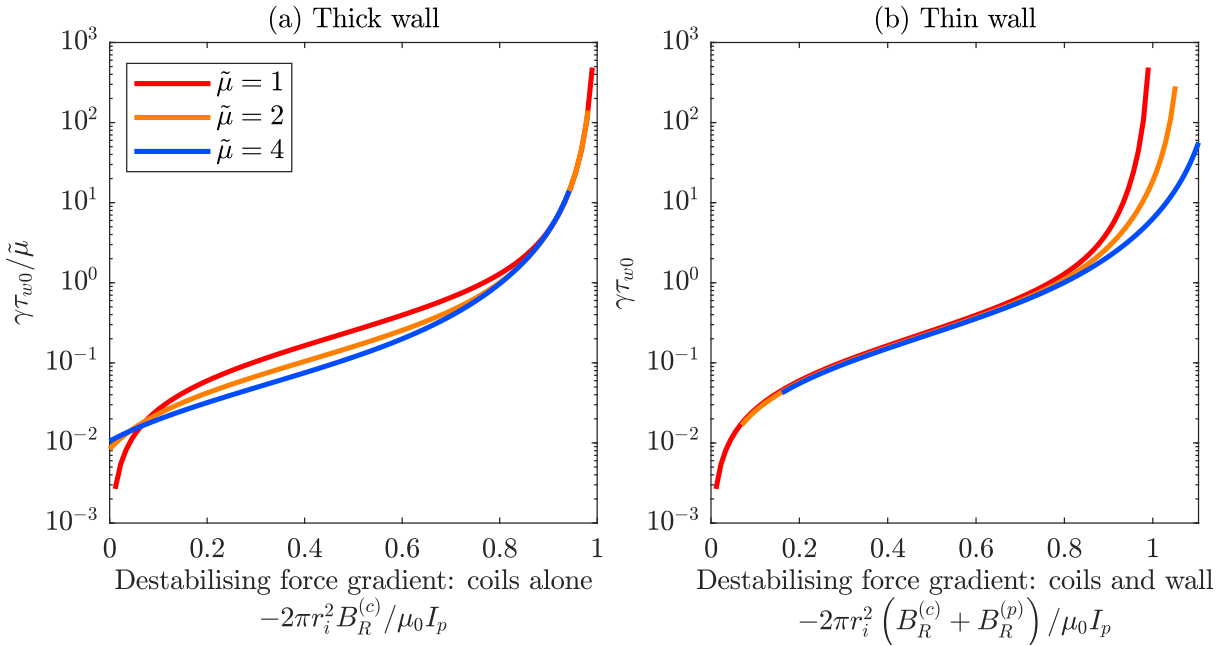


Figure 5: Vertical instability growth rate as a function of the destabilising force acting on the plasma, either (a) due to the external coils alone (equation 13), or (b) including the ferromagnetic force as well (equation 10). The former collapse in the limit of a thick wall, $\gamma\tau_{w0} \gg 1$ (note the vertical axis is scaled by $\tilde{\mu}$) whereas the latter collapse for a thin wall, $\gamma\tau_{w0} \ll 1$. Geometry is as figure 2 and the coil current I_c varies between 0 and I_p .

2.3.2 Slow (thin wall) instability

At the opposite extreme, we have the ‘slow’ limit, for which the instability growth rate is much less than the wall time ($\gamma\tau_{w0} \ll 1$), which amounts to a magnetic skin depth much greater than the wall thickness. Hence the perturbation due to the motion of the plasma occupies the whole volume of the conducting wall, and the interior field has time to adjust on account of the ferromagnetic effects of the wall. The destabilising force acting on the plasma is then a sum of that due to the divertor coils (13) and ferromagnetic wall (10). The stabilising effect of the currents induced in the wall, on the other hand, is independent of its magnetic permeability in this limit, as shown in appendix B. Hence the curves of γ against the *total* destabilising force gradient plotted in figure 5(b) converge for $\gamma\tau_{w0} \lesssim 1$. The interpretation here is that the instability growth rate also increases due to the ferromagnetic effect in the case of a thin wall, although the dependence of γ on $\tilde{\mu}$ is less trivial since it enters through the destabilising term (10). In fact, in the limiting case $\delta_w \ll s \ll r_w$, the force balance (22) becomes (see appendix B and equation 11)

$$\frac{\mu_0 I_p z_p}{2\pi r_w^2} \left(1 + \frac{2}{\mu_0 \sigma \gamma \delta_w r_w}\right)^{-1} + B_R^{(c)} - \frac{\mu_0 I_p z_p \delta_w}{4\pi r_w^3} \left(\tilde{\mu} - \frac{1}{\tilde{\mu}}\right) \approx 0. \quad (23)$$

Solving for the growth rate, we get

$$\gamma\tau_{w0} \approx \frac{\delta_w}{r_w} \left[\left(\frac{\delta_w}{r_w} \left(\tilde{\mu} - \frac{1}{\tilde{\mu}} \right) - \frac{4\pi r_w^2 B_R^{(c)}}{\mu_0 I_p z_p} \right)^{-1} - \frac{1}{2} \right]^{-1}. \quad (24)$$

As discussed previously, in order to maintain a specified plasma elongation in the presence of ferromagnetic material, the divertor coil current I_c must be increased such that $B_R^{(c)}$ is unchanged (in accordance with (13) or its approximation (14)), and hence the term containing $B_R^{(c)}$ in (24) can be thought of as independent of $\tilde{\mu}$. This expression therefore captures the dependence of the growth rate on the effective magnetic permeability

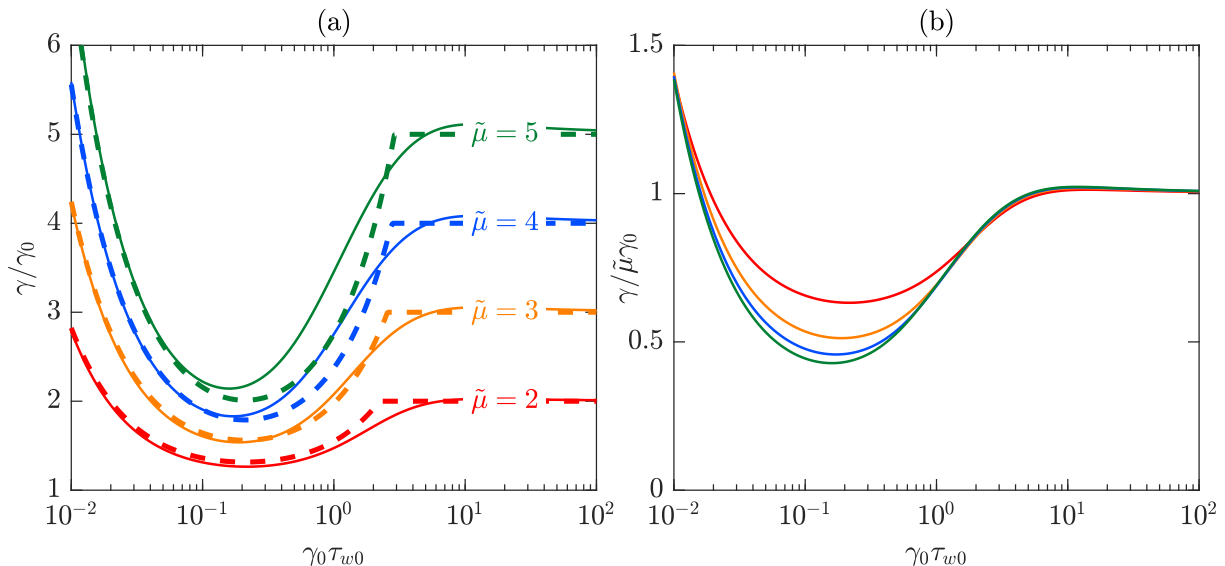


Figure 6: (a) Relative change in vertical instability growth rate γ as a function of its value in the absence of any ferromagnetic effects, γ_0 , keeping the externally-applied destabilising force gradient (and thus plasma elongation) constant. Solid lines show the exact result, and dashed lines the limiting forms for $\gamma\tau_{w0} \ll 1$ (see (25)) and $\gamma\tau_{w0} \gg 1$ ($\gamma = \tilde{\mu}\gamma_0$). (b) Exact result again, but normalised by $\tilde{\mu}$. The geometry is as figure 2.

(and wall geometry) at fixed plasma elongation, for the important limit of a (magnetically *and* geometrically) thin wall.

Making further use of the fact that $\delta_w \ll r_w$, we may usefully recast (24) in terms of γ_0 , the growth rate in the absence of any ferromagnetic effect:

$$\gamma\tau_{w0} \approx \gamma_0\tau_{w0} + \left(\tilde{\mu} - \frac{1}{\tilde{\mu}}\right) \left(\frac{\delta_w}{r_w} + \frac{\gamma_0\tau_{w0}}{2}\right)^2. \quad (25)$$

This relation is plotted as the dashed curves in figure 6(a), along with both the exact solution (as a solid line) and the opposite limit $\gamma\tau_{w0} \gg 1$ of section 2.3.1. It appears that the exact solution is well-approximated by (25) for $\gamma_0\tau_{w0} \lesssim 1$ and $\gamma = \tilde{\mu}\gamma_0$ for $\gamma_0\tau_{w0} \gtrsim 1$, particularly at the smaller values of $\tilde{\mu}$ applicable to tokamaks. This scheme therefore provides a simple means by which to adjust the values of growth rates calculated for a conventional conducting wall in order to account for the effects of ferromagnetism.

As we can see from figure 6(b), the effect is in general to increase growth rates by a factor on the order of the effective relative magnetic permeability $\tilde{\mu}$. The factor can be much larger than $\tilde{\mu}$ for instabilities with $\gamma_0\tau_{w0} \ll 1$, but this is a result of $\gamma_0 \rightarrow 0$ rather than $\gamma \rightarrow \infty$ and therefore not particularly worrying; physically, this represents the limit of the divertor coils being turned off so the only destabilising influence is ferromagnetic, in which case the growth rates are very slow anyway. The effect of ferromagnetism will be most pertinent for the fast, skin-effect dominated solutions, for which the vertical instability growth rate is already large ($\gamma_0\tau_{w0} \gtrsim 1$, i.e. $s \lesssim \delta_w$), but becomes even larger by a factor $\tilde{\mu}$, which could be ~ 2 in future tokamaks.

3 Tight aspect ratio tokamaks: a spherical model problem

Our second model problem considers an axisymmetric tokamak with the ferromagnetic conducting wall now taken to be a spherical shell which completely encloses the plasma. This choice is motivated by the need for a

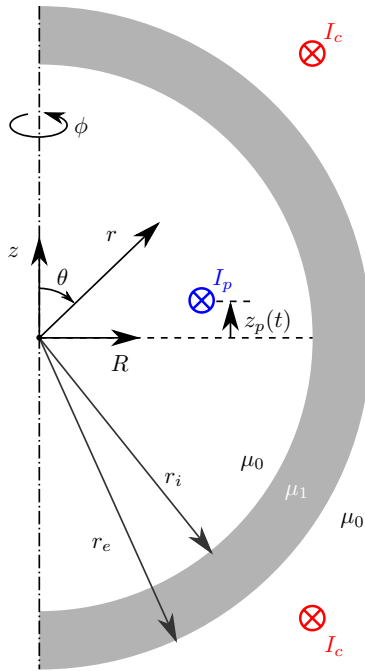


Figure 7: Schematic of the spherical model problem, showing geometry, parameters and co-ordinates.

greater understanding of ferromagnetic effects in spherical tokamaks, particularly their vertical stability characteristics at exaggerated elongations, acknowledging the importance of balancing divertor loads in double-null configurations [16, 8] and avoiding disruptions. Even in a conventional tokamak, simple geometrical considerations imply more ferromagnetic steel is likely to be located on the outboard side – say, for the structural components of tritium breeding modules [3] or toroidal field ripple reducing inserts [5, 6] – so this model problem provides useful insight in this context too.

It is to be expected that the paradigm of section 2, which makes a distinction between thick- and thin-walled instabilities, will carry over to this section as well, and indeed we will show this to be broadly the case. There are, however, a few new results which emerge in this second model problem, particularly with respect to the plasma’s radial equilibrium, and subtleties associated with the evaluation of the destabilising force on the plasma wire. This model is also much more flexible, with a range of plasma and coil locations possible, and should – by virtue of being axisymmetric rather than planar – have greater predictive capability. Since this model is very closely related to that of section 2, we proceed by analogy with the thread of that section, highlighting significant differences and new results when they arise. Symbols will be extensively re-used and have very similar meanings to section 2, being differentiated only by context. We also append certain equations with (cf. \sim) labels which relate them to analogous expressions in section 2.

The problem schematic is shown in figure 7. Since the wall is a spherical shell, the obvious co-ordinate system is spherical polars (r, θ, ϕ) with r the radial distance and θ the poloidal angle; the toroidal angle ϕ is ignorable because axisymmetry is assumed. We will use these interchangeably with cylindrical polar co-ordinates (R, z, ϕ) aligned with the symmetry axis. The ferromagnetic wall is again given a constant effective magnetic permeability, although this is now a fairly crude approximation because of the significant $1/R$ variation of the toroidal field in (1). (The choice is justified if the wall currents are concentrated on the outboard side, however.) The plasma wire is located at a cylindrical radius R_p and (assumed small) height z_p . Poloidal field coils are introduced outside of the conducting wall in up-down symmetric pairs, one example of which is shown in figure

7, but many such pairs will be included as desired. By convention, all currents are positive in the direction of increasing ϕ (into the page).

Rather than the flux function ψ of section 2, we now work with the vector potential $A(r, \theta, t)\mathbf{e}_\phi$ such that the poloidal flux density is

$$\mathbf{B} = \nabla \times (A\mathbf{e}_\phi) = \frac{1}{r \sin \theta} \frac{\partial}{\partial \theta} (A \sin \theta) \mathbf{e}_r - \frac{1}{r} \frac{\partial}{\partial r} (rA) \mathbf{e}_\theta, \quad (26)$$

(cf. 3) in which case the boundary conditions (2) at $r_{i,e}$ become

$$\left\langle \frac{\partial}{\partial \theta} (A \sin \theta) \right\rangle = \left\langle \frac{1}{\mu} \frac{\partial}{\partial r} (rA) \right\rangle = 0 \quad (27)$$

(cf. 4). Note also that the partial differential equation governing A is

$$\mu\sigma \frac{\partial A}{\partial t} = \frac{1}{r^2} \frac{\partial}{\partial r} \left(r^2 \frac{\partial A}{\partial r} \right) + \frac{1}{r^2} \frac{\partial}{\partial \theta} \left(\frac{1}{\sin \theta} \frac{\partial}{\partial \theta} (A \sin \theta) \right) \quad (28)$$

(cf. 15). As before, our approach is to first calculate the equilibrium field, which informs the destabilising force, then the stabilising time-dependent field due to the displacement of the plasma wire vertically as $e^{\gamma t}$. Assuming a massless plasma, the net Lorentz force from these two fields much vanish at its location, a criterion which gives an equation for the instability growth rate γ .

3.1 Equilibrium solution

We begin by solving for the equilibrium magnetic flux density, which satisfies the steady version of (28) subject to the boundary conditions (27). Again, contributions due to the plasma wire and external coil pairs may be treated independently then summed.

3.1.1 Plasma wire

We first derive the solution due to the plasma wire at an arbitrary cylindrical radius R_p and height z_p (equivalently, spherical radius r_p and poloidal angle θ_p), in analogy with section 2.1.1. In the absence of any ferromagnetic effects, the vector potential due to a thin circular hoop carrying a constant current, which zeros the right-hand side of (28), may be written as the infinite sum [10]

$$A^{(p)} = \sum_{\ell=1}^{\infty} \frac{\mu_0 I_p \sin^2 \theta_p}{2\ell(\ell+1)} \frac{r_p r_{\leq}^{\ell}}{r_{>}^{\ell+1}} P_{\ell}^1(\cos \theta) P_{\ell}^1(\cos \theta_p) \quad (29)$$

(cf. 5) where r_{\leq} is the lesser/greater of r and r_p , and $P_{\ell}^1(\cdot)$ is the associated Legendre polynomial of degree ℓ and order 1. Introducing the ferromagnetic wall, we then have the general solution

$$A^{(p)} = \sum_{\ell=1}^{\infty} \hat{A}_{\ell}^{(p)}(r) P_{\ell}^1(\cos \theta) \quad (30)$$

(cf. 6) where

$$\hat{A}_{\ell}^{(p)} = C_{\ell}^{(p)} \frac{r_i^{\ell+1} r_{\leq}^{\ell}}{r_p^{\ell} r_{>}^{\ell+1}} + D_{\ell}^{(p)} \left(\frac{r}{r_i} \right)^{\ell} \quad (31)$$

(cf. 8). The coefficients $C_{\ell}^{(p)}$ and $D_{\ell}^{(p)}$ take on different values in the three domains ($i/w/e$); we can see by comparison with (29) that the known internal coefficients are

$$C_{\ell}^{(p,i)} = \frac{\mu_0 I_p \sin^2 \theta_p}{2\ell(\ell+1)} \left(\frac{r_p}{r_i} \right)^{\ell+1} P_{\ell}^1(\cos \theta_p) \quad (32)$$

(cf. 9), and furthermore any valid solution must vanish at infinity, implying $D_{\ell}^{(p,e)} = 0$. The remaining coefficients are solved for in appendix C.1 by application of the boundary conditions (27). A simple example

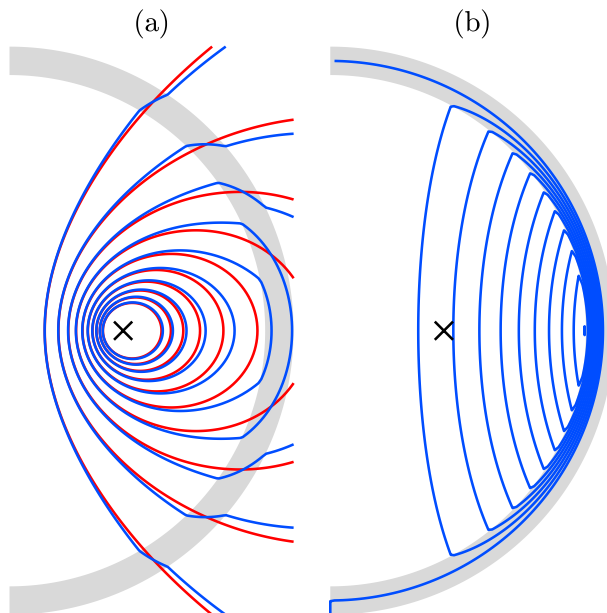


Figure 8: Equilibrium magnetic flux surfaces due to a plasma wire. (a) Comparison between ferromagnetic ($\tilde{\mu} = 3$, blue) and non-ferromagnetic ($\tilde{\mu} = 1$, red) cases. (b) Difference between the two, i.e. the field ‘due to the wall’. Geometry is $r_i = 0.9r_e$, $R_p = 0.4r_e$ and $z_p = 0$; the black cross represents the plasma wire.

magnetic flux distribution is shown in figure 8, with a comparison to the non-ferromagnetic solution.

Having derived the vector potential due to the reaction of the ferromagnetic wall to the plasma wire, the next step is to evaluate the magnetic flux components at the location of the plasma itself, since they will give the resulting Lorentz force acting upon it. The natural choice of equilibrium is a symmetric one in which the plasma wire is sited in the midplane, $z_p = 0$, in which case the vertical field at the plasma location is

$$B_z^{(p)} \Big|_{\substack{R=R_p \\ z=z_p=0}} = \sum_{\substack{\ell=1 \\ \ell \text{ odd}}}^{\infty} \frac{\mu_0 I_p}{2\ell R_p} \frac{D_\ell^{(p,i)}}{C_\ell^{(p,i)}} \left(\frac{R_p}{r_i} \right)^{2\ell+1} [P_\ell^1(0)]^2, \quad (33)$$

with $D_\ell^{(p,i)}/C_\ell^{(p,i)}$ from (82). Clearly, unlike the cylindrical model, the equilibrium field due to the ferromagnetic wall has a non-zero vertical component at the plasma location, and hence exerts a horizontal force upon it, with a sign such that the two attract each other (i.e. the wall pulls the plasma radially outwards). We postpone discussion of the effect of this on plasma equilibrium to section 3.1.3, once the external coil fields have been evaluated.

Because our equilibrium is symmetric about the midplane, the radial magnetic flux at the plasma location is zero and hence there is no vertical Lorentz force acting on the plasma in equilibrium. However, when the plasma wire is displaced vertically by a small amount (i.e. at the onset of a VDE) it will experience a vertical force as a result of its own equilibrium field (ignoring induced currents in the wall for the time being). To leading order in the plasma height z_p , this can be separated into two components. The first is due to the curvature of the equilibrium field produced by the ferromagnetic wall — see the field lines of figure 8(b). It is

$$\frac{\partial}{\partial z} \left(B_R^{(p)} \Big|_{\substack{R=R_p \\ z_p=0}} \right)_{z=0} = \sum_{\substack{\ell=3 \\ \ell \text{ odd}}}^{\infty} \frac{\mu_0 I_p (\ell-1)}{2\ell R_p^2} \frac{D_\ell^{(p,i)}}{C_\ell^{(p,i)}} \left(\frac{R_p}{r_i} \right)^{2\ell+1} [P_\ell^1(0)]^2. \quad (34)$$

This contribution is not present in the cylindrical model of section 2.1.1 because the equilibrium field due to the wall is zero at the origin when $z_p = 0$. Its effect here is always vertically stabilising – as is evident from figure

8(b), considering that the direction of magnetic flux must be such that the horizontal force on the plasma is radially outward – but because the force arises from field line curvature this stabilisation comes at the cost of reduced plasma elongation. Note that this contribution is also independent of the instability growth rate, and so is most simply thought of as a modification to the external coils’ destabilising force gradient.

The second contribution, which is familiar from the cylindrical problem (section 2.1.1), is only present in the limit of a slow-growing (or thin-wall, $\gamma\tau_{w0} \ll 1$) instability. It is the change in the equilibrium radial field in the midplane ($z = 0$) due to a slight excursion of the plasma wire from $z_p = 0$, which is

$$\frac{\partial}{\partial z_p} \left(B_R^{(p)} \Big|_{R=R_p} \right)_{z_p=0} = \sum_{\substack{\ell=2 \\ \ell \text{ even}}}^{\infty} -\frac{\mu_0 I_p \ell(\ell+1)}{2R_p^2} \frac{D_\ell^{(p,i)}}{C_\ell^{(p,i)}} \left(\frac{R_p}{r_i} \right)^{2\ell+1} [P_\ell^0(0)]^2 \quad (35)$$

(cf. 10) — observe the subtle difference between the derivatives in (34) and (35). This represents the additional destabilising force due to the effects of ferromagnetism in the case $\gamma\tau_{w0} \ll 1$, as discussed in section 2.3.2, which (unlike the first component (34)) is not directly linked to the plasma elongation. If the wall is also geometrically thin ($\delta_w \ll r_i$), and we may approximate the sum in (35) by the first two terms only on the grounds that the plasma wire is reasonably far from the wall, then we may use (83) to find

$$\Delta\hat{n} = -\frac{R_p}{B_z} \frac{\partial}{\partial z_p} \left(B_R^{(p)} \Big|_{R=R_p} \right)_{z_p=0} \approx \frac{3}{10} \frac{\mu_0 I_p}{B_z R_p} \left(\frac{R_p}{r_i} \right)^5 \frac{\delta_w}{r_i} \Delta\mu \quad (36)$$

(cf. 11), where

$$\Delta\mu = \left(1 - \frac{1}{\tilde{\mu}} \right) \left[(2\tilde{\mu} + 3) + \frac{25}{12} (4\tilde{\mu} + 5) \left(\frac{R_p}{r_i} \right)^4 \right]. \quad (37)$$

Note that (36) has a very strong dependency upon the distance between the plasma and wall (i.e. R_p/r_i), and that we have expressed it as a modification $\Delta\hat{n}$ to the field index \hat{n} ; Tsuzuki *et al.* [17] report a relative change in this value of a few percent due to the ferromagnetic wall when the plasma is slightly displaced vertically. Using relevant parameters for the JFT-2M tokamak ($r_i \approx 1.7\text{m}$, $R_p \approx 1.3\text{m}$, $\delta_w \approx 8\text{mm}$, $\tilde{\mu} \sim 2 - 4$ and (from [18]) $\xi \sim 0.2 - 0.7$), we consistently estimate $\Delta\hat{n}/\hat{n} \sim 0.4 - 3.6\%$ using the expression above.

3.1.2 External coils

The equilibrium field due to an external coil pair is comparatively straightforward. The general solution is very similar to (31), only now with a source external to the wall:

$$\hat{A}_\ell^{(c)} = C_\ell^{(c)} \left(\frac{r_i}{r} \right)^{\ell+1} + D_\ell^{(c)} \frac{r_c^{\ell+1} r_{\leq}^{\ell}}{r_i^{\ell} r_{>}^{\ell+1}}, \quad (38)$$

where r_{\leq} is the lesser/greater of r and r_c , and the coefficients take on different values in the various domains. For regularity at the origin the $C_\ell^{(c,i)}$ must be zero, whereas the external coefficients are

$$D_\ell^{(c,e)} = \frac{\mu_0 I_c \sin^2 \theta_c}{\ell(\ell+1)} \left(\frac{r_i}{r_c} \right)^\ell P_\ell^1(\cos \theta_c) \quad (39)$$

(cf. 12) for ℓ odd, and zero for ℓ even. The solution for the remaining coefficients is given in appendix C.2. The vertical component of magnetic flux density at the plasma location is

$$B_z^{(c)} \Big|_{R=R_p} = \sum_{\substack{\ell=1 \\ \ell \text{ odd}}}^{\infty} \frac{\mu_0 I_c \sin^2 \theta_c}{\ell R_p} \frac{D_\ell^{(c,i)}}{D_\ell^{(c,e)}} \left(\frac{R_p}{r_c} \right)^\ell P_\ell^1(\cos \theta_c) P_\ell^1(0) \quad (40)$$

with $D_\ell^{(c,i)}/D_\ell^{(c,e)}$ from (89). Through this term, external coils may exert a force upon the plasma in order to maintain radial equilibrium. As for vertical stability, the force gradient is provided by the curvature term

$$\left. \frac{\partial B_R^{(c)}}{\partial z} \right|_{\substack{R=R_p \\ z=0}} = \sum_{\substack{\ell=3 \\ \ell \text{ odd}}}^{\infty} \frac{\mu_0 I_c (\ell - 1) \sin^2 \theta_c}{\ell R_p^2} \frac{D_\ell^{(c,i)}}{D_\ell^{(c,e)}} \left(\frac{R_p}{r_c} \right)^\ell P_\ell^1(\cos \theta_c) P_\ell^1(0) \quad (41)$$

(cf. 13). Note this term may be stabilising, destabilising, or neutral depending on the precise location of the external coil pair.

3.1.3 Radial force balance

Whereas the cylindrical model problem of section 2 was trivially in force equilibrium before the VDE, by virtue of the externally-applied magnetic flux being zero at the origin, for the spherical version the equilibrium configuration must obey a radial force balance. That is, the plasma hoop force and ferromagnetic pull of the wall (both of which act radially outwards) must be balanced by the externally-applied vertical field:

$$B_z^{hoop} + B_z^{(p)} + \sum_c B_z^{(c)} = 0, \quad (42)$$

wherein the plasma and coil fields come from (33) and (40) respectively, and we have allowed for the inclusion of multiple external coils. In the limit of a large aspect ratio plasma (an approximation no worse than taking the plasma to be a thin wire), the vertical field required to balance the plasma hoop force is [19]

$$B_z^{hoop} = \frac{\mu_0 I_p}{4\pi R_p} \left(\ln \frac{8R_p}{a_p} + \Lambda - \frac{1}{2} \right), \quad (43)$$

where a_p is the plasma minor radius, and $\Lambda = \beta_{pol} + \frac{1}{2}l_i - 1$ for a plasma of poloidal beta β_{pol} and internal inductance l_i ; for simplicity, the bracketed quantity in (43) is assumed independent of R_p .

We explore modification of the radial force balance by means of a simple example, in which the current in a single external coil pair and the plasma radius R_p are both varied in search of equilibrium solutions. We choose a wall with $r_i = 0.9r_e$ and $\tilde{\mu} = 3$, with the external coils placed as a Helmholtz pair at $R_c = 1.2r_e$, $z_c = \pm 0.6r_e$. Figure 9 shows the left-hand side of the force balance (42) as a function of R_p for various coil currents I_c ; this quantity is zero in equilibrium. Dashed orange lines show the non-ferromagnetic ($\tilde{\mu} = 1$) case for comparison. First consider the topmost pair of lines, with no externally-applied field. The non-ferromagnetic case is just (43), which drops off as $1/R_p$, whereas the ferromagnetic case deviates as R_p approaches r_i due to the addition of the $B_z^{(p)}$ term (33), with the outward force on the plasma increasing considerably as it is pulled towards the wall. Since both forces are outwards an equilibrium is unachievable. Addition of an external field with I_c negative, however, pushes the plasma inwards i.e. lowers the curves in figure 9 to such a point that solutions to (42) may exist. These are indicated by filled triangles. In the non-ferromagnetic case there is only ever one such equilibrium, which moves inwards as $|I_c|$ increases. If the wall is ferromagnetic, for a given I_c this first equilibrium either moves slightly outwards (see the curves for $|I_c| \geq 0.75I_p$) or ceases to exist at all (see the curves for $I_c = -0.5I_p$). Furthermore, a second equilibrium comes into being at larger R_p (denoted by upward-pointing triangles), but it is unstable because a small displacement either outwards or inwards from the equilibrium R_p would result in a net force on the plasma which reinforces that motion. Clearly, in the ferromagnetic case there is a maximum possible R_p – or equivalently, a minimum requirement on $|I_c|$ – for stable equilibrium solutions to exist. (In this example these are $0.729r_i$ and $0.674I_p$ respectively — see the black cross in figure 9.) Note that equilibria with R_p just below this value are likely to be metastable; although linearly stable to small displacements, a larger outwards perturbation could take the plasma past the unstable equilibrium location, thereby causing it to be pulled inexorably into the wall by their mutual ferromagnetic

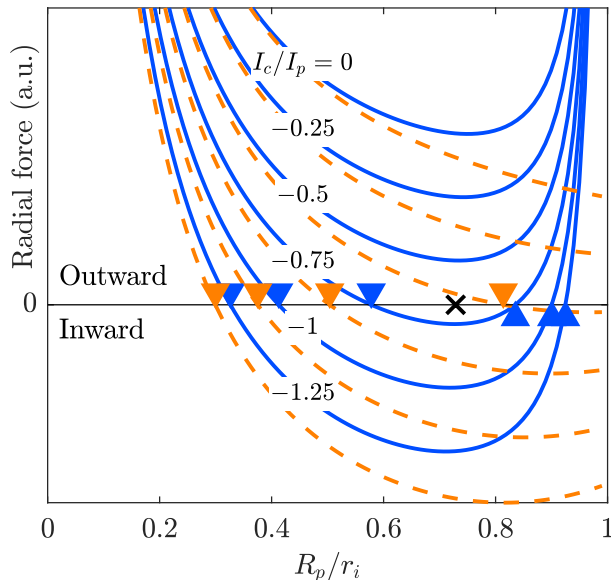


Figure 9: The net radial force on the plasma (42) as a function of major radius at various values of external coil current I_c . The parameters are $r_i = 0.9r_e$, $R_c = 1.2r_e$, $z_c = \pm 0.6r_e$, $\tilde{\mu} = 3$ and we use $\Lambda = 0.25$, $R_p/a_p = 2$. Solid blue lines show the ferromagnetic case, with dashed orange lines the $\tilde{\mu} = 1$ equivalent for comparison. Triangles denote equilibria: downward-pointing for stable, upward for unstable. The black cross is the maximum stable equilibrium. Labels ‘outward’ and ‘inward’ indicate the direction of the net force.

attraction.

A natural next question is, how might equilibria with a distributed plasma current be affected by significant amounts of ferromagnetic material on the outboard side? Although a full answer to this question is beyond our scope (but see existing discussions of the modification of plasma shape by a ferromagnetic core [20, 21] and its inclusion in equilibrium reconstruction [22, 23, 24]), it appears that currents flowing close to the wall would be strongly attracted towards it. This may place a limit on how close the LCFS could get to the ferromagnetic wall, particularly for plasmas of low internal inductance.

3.1.4 Ferromagnetic equilibria

We are now in a position to calculate the equilibrium magnetic flux from both a plasma wire and a number of external coil pairs; figure 10 shows a few examples, for a reasonably thick wall of moderate effective magnetic permeability. A minimal external coil set is used, with ‘vertical field’ coils on the outboard side providing the bulk of the radial force and ‘divertor’ coils directly above and below the plasma wire controlling the elongation. The current I_c^{div} in this latter pair is varied between the panes of figure 10 in order to produce different field shapes; note how the LCFS encloses a smaller area as I_c^{div} increases, but also that its elongation κ increases. (A nominal inboard limiter has been included to keep the plasma shape plausible — see figure 10(a).) As found in the cylindrical equilibrium (section 2.1.3), elongation is strongly correlated with the destabilising force gradient for an X-point LCFS. (This has been checked, but is not shown because the plot essentially duplicates figure 3.) The difference here is that the destabilising force gradient includes a contribution due to the reaction of the wall to the plasma wire (see section 3.1.1) as well as that due to the external coils.

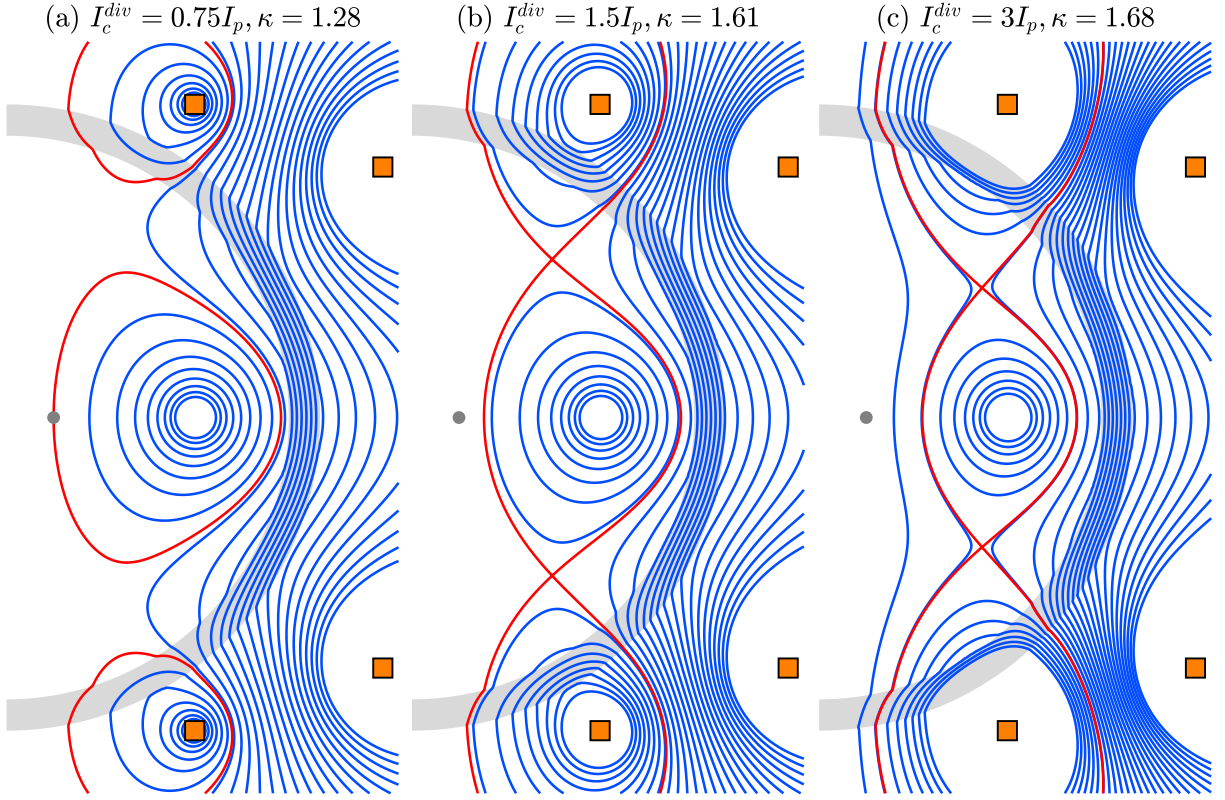


Figure 10: Equilibrium poloidal magnetic flux surfaces for various divertor currents. The wall, shown in grey, has $r_i = 0.9r_e$ and $\bar{\mu} = 3$. Coils are plotted as orange squares; the vertical field coil current is adjusted in order to keep $R_p = 0.6r_e$ constant. Red curves show the LCFS, defined either by the X-point or the inboard limiter at $R = 0.15r_e$ (grey dot).

3.2 Time-dependent field

We now calculate the vector potential which satisfies (28) with the time derivative reinstated within the volume of the conducting ferromagnetic wall; as in section 2.2, we let the plasma height grow as $z_p \propto e^{\gamma t}$ and calculate the induced currents in the wall, then the corresponding back-reaction upon the plasma wire. The linearised perturbation to the vector potential has a general series solution of the form

$$a(r, \theta, t) = \sum_{\substack{\ell=2 \\ \ell \text{ even}}}^{\infty} \hat{a}_\ell(r) e^{\gamma t} P_\ell^1(\cos \theta) \quad (44)$$

(cf. 17), where

$$\hat{a}_\ell e^{\gamma t} = \begin{cases} c_\ell^{(i)} \frac{r_i^{\ell+1} r_{\leq}^\ell}{R_p^\ell r_{>}^{\ell+1}} + d_\ell^{(i)} \left(\frac{r}{r_i}\right)^\ell, & (i) \\ c_\ell^{(w)} i_\ell(y) + d_\ell^{(w)} k_\ell(y), & (w) \\ c_\ell^{(e)} \left(\frac{r_i}{r}\right)^{\ell+1}, & (e) \end{cases} \quad (45)$$

(cf. 18). Here, $i_\ell(y) = (\pi/2y)^{1/2} I_{\ell+1/2}(y)$ and $k_\ell(y) = (\pi/2y)^{1/2} K_{\ell+1/2}(y)$ are modified spherical Bessel functions and r_{\leq} is the lesser/greater of r and R_p . By comparison with a Taylor expansion of the plasma wire solution (29) about $z_p = 0$, it can be seen that

$$c_\ell^{(i)} = \frac{\mu_0 I_p z_p}{2} \frac{R_p^\ell}{r_i^{\ell+1}} P_\ell^0(0), \quad (46)$$

whereas the remaining coefficients are derived through application of the boundary conditions (27) at the interior-wall and wall-exterior interfaces (see appendix C.3). Most importantly, the resulting horizontal magnetic

flux density at the plasma location is, to leading order in z_p ,

$$b_R = \sum_{\substack{\ell=2 \\ \ell \text{ even}}}^{\infty} -\frac{\mu_0 I_p z_p}{2R_p^2} \ell(\ell+1) \frac{d_\ell^{(i)}}{c_\ell^{(i)}} \left(\frac{R_p}{r_i}\right)^{2\ell+1} [P_\ell^0(0)]^2 \quad (47)$$

(cf. 19), with $d_\ell^{(i)}/c_\ell^{(i)}$ given by (96)-(97). This expression gives the vertical Lorentz force acting on the displaced plasma wire due to the presence of the wall.

Having learnt in section 2 that distinguishing between fast and slow (or thick- and thin-wall) instabilities proves a useful paradigm for understanding the ferromagnetic vertical stability problem, we adopt the same approach here. First taking the limit of a magnetically thick wall ($s \ll \delta_w$ or $\gamma\tau_{w0} \gg 1$), we have

$$\frac{d_\ell^{(i)}}{c_\ell^{(i)}} \approx -1 + \frac{(2\ell+1)\tilde{\mu}}{y_i} + \mathcal{O}(y_i^{-2}) \quad (48)$$

(cf. 20). Once again, this makes b_R a function of $\tilde{\mu}$ and γ only in the combination $\gamma/\tilde{\mu}$, since $y_i/\tilde{\mu} = r_i\sqrt{\mu_0\sigma\gamma/\tilde{\mu}}$, and hence (for a given plasma elongation) we can expect growth rates to grow by a factor $\tilde{\mu}$ when the wall may be considered magnetically thick. Note that taking just the leading-order term in (48) gives the maximum possible stabilising wall force $b_{R,max}$ (i.e. the ideal wall limit); destabilising force gradients which exceed this value will lead to unstable growth on the Alfvén time.

On the other hand, if the wall is magnetically thin then the vertical force is the sum of the quasi-steady destabilising ferromagnetic force (35) and a permeability-independent stabilising term due to the induced wall currents:

$$\frac{d_\ell^{(i)}}{c_\ell^{(i)}} \approx \frac{D_\ell^{(p,i)}}{C_\ell^{(p,i)}} - \left(1 + \frac{2\ell+1}{\mu_0\sigma\gamma\delta_w r_w}\right)^{-1}. \quad (49)$$

See (82) (or (83) in the limit $\delta_w \ll r_w$) for $D_\ell^{(p,i)}/C_\ell^{(p,i)}$. The derivation of the second term very closely follows the equivalent cylindrical version (appendix B).

3.3 Calculation of growth rate

We are now in a position to calculate the vertical instability growth rate of a plasma wire within a conducting, ferromagnetic spherical shell, by solving the massless plasma force balance equation

$$b_R + z_p B'_R = 0 \quad (50)$$

(cf. 22), where for brevity we define

$$B'_R = \frac{\partial}{\partial z} \left(B_R^{(p)} \Big|_{z_p=0} + \sum_c B_R^{(c)} \right)_{\substack{R=R_p \\ z=0}} \quad (51)$$

as the total vertical force gradient due to the curvature of equilibrium field lines — see (34) and (41) for definitions of the plasma and coil contributions respectively. The term in (50) associated with the time-dependent response of the wall, $b_R(\gamma)$, is given by (47).

Before we calculate any growth rates, it is worthwhile summarising the forces which act on the plasma at the onset of a ferromagnetic VDE. These can be broken down into four contributions; two associated with the equilibrium field and two with the time-dependent field. They are:

1. The equilibrium curvature force due to external coil pairs, given by (41). This may be stabilising or destabilising, depending upon the exact arrangement of the coils, although for configurations where vertical stability is an issue will inevitably be destabilising. Determined as a sum over any number of coil pairs, but because our model problem treats the plasma as a wire, only its point value is relevant.
2. The equilibrium curvature force due to the response of the wall to the wire itself, given by (34), or see figure 8(b). This is always vertically stabilising, but only because it reduces the plasma elongation. Although both this term and (1.) are nominally functions of $\tilde{\mu}$, their sum (51) will be approximately fixed for a plasma of given elongation — the currents in the poloidal field coils will simply have to be adjusted in order to achieve it.
3. The quasi-steady destabilising ferromagnetic force (35), which is the force the wall would exert upon the plasma wire if it were held stationary at a small height z_p above the midplane. If the VDE occurs quickly relative to the resistive wall time ($\gamma\tau_{w0} \gg 1$), then the internal field does not have time to reconfigure to the ferromagnetic equilibrium of section 3.1.1 and so this term does not contribute. On the other hand, for slow-growing instabilities ($\gamma\tau_{w0} \ll 1$) this term constitutes an additional destabilising influence which is independent of the plasma elongation.
4. The force due to currents induced in the conducting wall, given by (47) with the contribution from (3.) subtracted out. This term is always stabilising, but has a character which depends upon the instability growth rate. If it's fast, this contribution becomes (48), which is a function of $\gamma/\tilde{\mu}$ only. For slow growth, however, the induced currents are approximately independent of the magnetic permeability, and given by the second term in (49).

In summary, (1.) and (2.) act independently of the growth rate and are tied to the plasma elongation. For $\gamma\tau_{w0} \gg 1$, (3.) is negligible whereas (4.) is modified by $\gamma \rightarrow \gamma/\tilde{\mu}$ for non-unity $\tilde{\mu}$. For $\gamma\tau_{w0} \ll 1$, (3.) provides an additional destabilising ferromagnetic force but (4.) is unchanged by the existence of ferromagnetism. In either case, although the reasons for it are subtly different, the growth rate is expected to increase with $\tilde{\mu}$.

Figure 11 shows the calculated growth rate as a function of the destabilising force, and is the analogue of figure 5 in the cylindrical model problem — once again, the curves coalesce for $\gamma\tau_{w0} \gg 1$ in the thick-wall limit (a) and $\gamma\tau_{w0} \ll 1$ in the thin-wall limit (b). In the latter case, it is possible to derive an approximate expression for the growth rate by using the thin-wall limits (35) and (49) in the massless force balance (50) to obtain, for $\delta_w \ll s \ll r_w$,

$$\gamma\tau_{w0} \approx \frac{\delta_w}{r_w} \left[\left(2 \frac{\delta_w}{r_w} \Delta_\mu - \frac{20}{3} \frac{B'_R r_i^5}{\mu_0 I_p R_p^3} \right)^{-1} - \frac{1}{5} \right]^{-1} \quad (52)$$

(cf. 24) — see (37) for Δ_μ . If the destabilising force due to the equilibrium field line curvature B'_R is kept constant as $\tilde{\mu}$ varies, then the growth rate is given approximately by

$$\gamma\tau_{w0} \approx \gamma_0\tau_{w0} + 2\Delta_\mu \left(\frac{\delta_w}{r_w} + \frac{\gamma_0\tau_{w0}}{5} \right)^2 \quad (53)$$

(cf. 25). Plots of γ/γ_0 as a function of $\gamma_0\tau_{w0}$ using this formula show an agreement with the exact calculation and a functional dependence on γ_0 which is very similar to the cylindrical version of figure 6. Equation (53) for $\gamma_0\tau_{w0} \lesssim 1$ (and $\gamma = \tilde{\mu}\gamma_0$ for $\gamma_0\tau_{w0} \gtrsim 1$) therefore provides a convenient way to estimate the change in instability growth rate accountable to ferromagnetic effects, for a spherical tokamak plasma of specified elongation κ and major radius R_p .

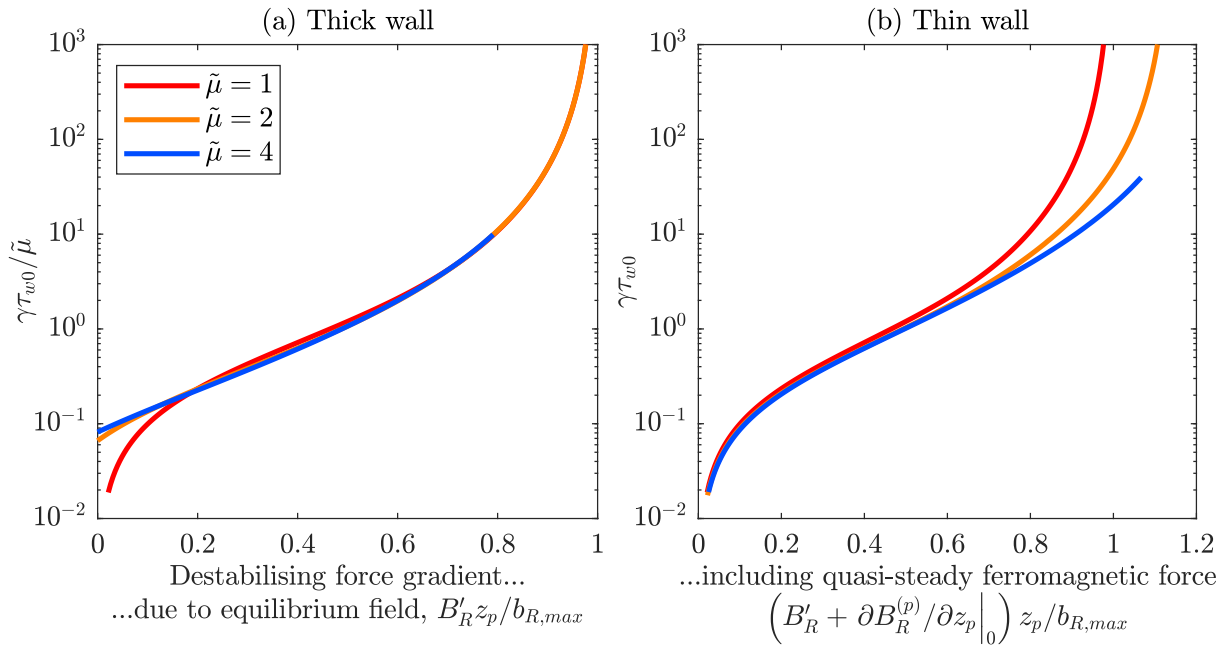


Figure 11: Vertical instability growth rate as a function of the destabilising force acting on the plasma, either (a) due to the equilibrium field line curvature (equation 51), or (b) including the ferromagnetic force as well (right pane, equation 35). The former collapse in the limit of a thick wall, $\gamma\tau_{w0} \gg 1$ (note the vertical axis is scaled by $\tilde{\mu}$) whereas the latter collapse for a thin wall, $\gamma\tau_{w0} \ll 1$. Geometry is as figure 10 with the divertor coil current I_c^{div} varying between 0 and $3.5I_p$ whilst the vertical field coil current is adjusted such that radial force balance (42) is maintained. (cf. figure 5)

4 Discussion

We have explored the equilibrium and vertical stability characteristics of tokamaks with ferromagnetic walls through two related analytical models in cylindrical (section 2) and spherical (section 3) geometries. The former is more straightforward and so provides a useful handle on the problem, but we concentrate our discussion on the latter because of its richer physics content.

4.1 Equilibrium

From the study of radial force balance (section 3.1.3), it is apparent that the presence of significant ferromagnetic material has a non-negligible effect upon the plasma equilibrium, with the mutual attraction between the two increasing demand on the vertical field coils in order to maintain radial force equilibrium (see figure 9 and previous experimental findings [17]). The effects are magnified the closer the plasma gets to the wall, to such a degree that radial equilibria with R_p above a certain critical value become unstable, at least in this model; for a distributed plasma current the story may be different, but such an investigation lies beyond the present scope. Ferromagnetic effects also increase the divertor current necessary to obtain a certain elongation for a given plasma current and position, because the wall's response to the plasma (figure 8, section 3.1.1) acts to reduce elongation (i.e. is vertically stabilising). For these two reasons at least, it is clear that ferromagnetic effects cannot be neglected in equilibrium calculations regarding tokamaks containing significant quantities of ferritic steel, and the calculations above should provide a useful first-order estimate of the required modifications to the applied external currents. Indeed, the present work could form the basis for a next-level equilibrium solver which considers distributed plasma currents, multiple poloidal field coils, and additional passive conducting structures.

4.2 Vertical instability

The focus of our study has been on the modification to the vertical instability growth rate for a conducting wall with an effective relative magnetic permeability $\tilde{\mu} \sim 2 - 4$, as compared to the non-ferromagnetic case. Limits for fast and slow instabilities, similar to FRWMs [11], have been established (section 3.3, figure 11) to guide understanding of the physical mechanisms at play. Fast instabilities are skin-effect dominated and the influence of ferromagnetism is to reduce penetration of magnetic flux into the wall, weakening its stabilising response by a factor $\tilde{\mu}$ (again, this is analogous to FRWMs [15]). Slow instabilities allow time for the ferromagnetic response to the plasma's motion to rearrange itself such that it stays close to the equilibrium configuration of section 3.1.1, and therefore provides an additional destabilising force with non-trivial dependence upon γ and $\tilde{\mu}$.

Whilst these limiting cases are useful for establishing intuition, a real tokamak is likely to operate in a regime where $\gamma\tau_{w0}$ is of order unity; smaller values correspond to meagre plasma elongation and hence suboptimal performance, whereas pushing the elongation and therefore increasing the growth rate will make the plasma uncontrollable [25]. With this in mind, the full expression for the stabilising wall force (see section 3.2 and appendix C.3) should be used in order to estimate growth rates consistently (though note that the thin-wall approximation (52) works surprisingly well at intermediate $\gamma\tau_{w0}$, akin to figure 6). The upshot is that changing the steel to ferromagnetic, whilst keeping everything else (geometry, plasma elongation, and electrical conductivity) constant results in an increase to the growth rate on the order of the effective magnetic permeability — see figure 6(b). This enhanced vertical instability must be accommodated by an improvement in the performance of active vertical control systems, even as ferromagnetic effects also erode their influence on the tokamak interior. The issue awaits future detailed study, but it seems that special care must be taken in the design of vertical control systems for tokamaks containing ferritic steels.

4.2.1 Induced current distribution

The spatial structure of currents induced within the wall during a VDE will be of much interest when designing ferritic structural components for tokamaks; this is shown in figure 12 for the VDE onset of the same equilibria plotted in figure 10 — recall the magnetic permeability is $\tilde{\mu} = 3$ and the divertor coil current is varied with the plasma major radius being held constant. A weak divertor current (figure 12(a)) implies a gentle destabilising force gradient and therefore a slow-growing instability, such that $\gamma\tau_{w0} \ll 1$ and the currents within the wall occupy its entire thickness. On the other hand, if the divertor current is strong (figure 12(c)) then the growth rate is large ($\gamma\tau_{w0} \gg 1$) because the destabilising force gradient is more severe. The perturbed current density is confined to a narrow skin of thickness $s \ll \delta_w$ and the associated magnetic flux is almost completely interior. An intermediate — probably most reactor-relevant — case with $\gamma\tau_{w0} \sim 1$ is shown in figure 12(b).

Observe that the induced current density is generally found in the outboard region of the wall, relatively close to the midplane. Recall that, in this model problem, our choice of a constant effective magnetic permeability $\tilde{\mu}$ neglects its true dependency on the toroidal magnetic flux (see (1)), which itself varies as $1/R$. However, since the induced currents are biased towards the outboard midplane it seems reasonable to use the effective permeability there (at $R = r_i$, say) for the entire wall, at least as a first approximation. Furthermore, this suggests there should not be any substantial modification to these results when the wall is not a full spherical shell, but rather has coverage only on a limited portion of the outboard side, as for existing tritium breeding region designs [26, 27]. We may add the caveats, however, that a distributed plasma might induce wall currents further from the midplane, and that toroidally discrete wall elements may be different [28].

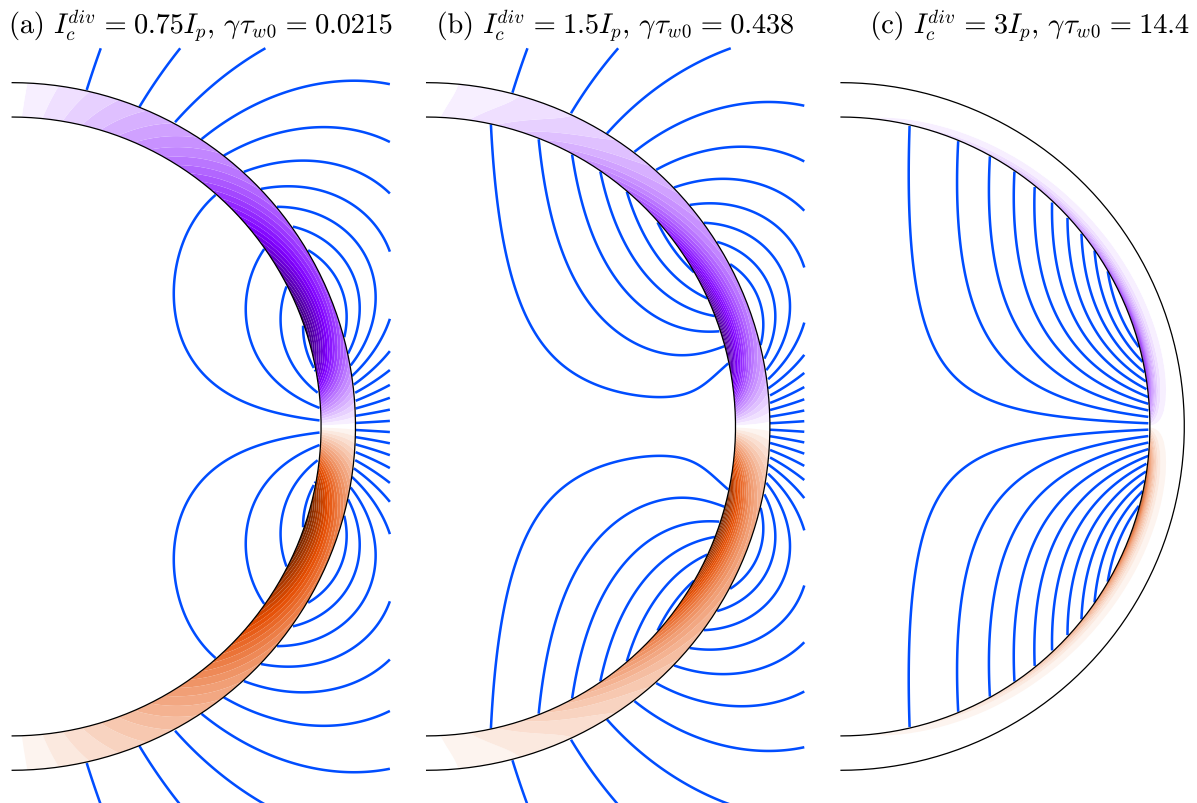


Figure 12: Induced field at VDE onset for the equilibria of figure 10. Solid colour shows the toroidal current density distribution within the conducting wall (orange positive, purple negative with respect to I_p) normalised to its maximum absolute value. Contour lines show poloidal magnetic flux surfaces in the vacuum regions associated with this current distribution.

4.3 Future work

The analytical models here naturally have limitations which might be usefully addressed in future studies — as discussed above, the simple geometry, constant $\tilde{\mu}$, singular plasma current, and lack of any other passive conductors or control coils may all be cited as shortcomings, and one might add to this list the enforced up-down symmetry, or the choice of a linearised perturbation. Perhaps one of the most important inaccuracies is the choice of a toroidally continuous wall, since tritium breeding is likely to be done in modules with ferritic structural elements which do not necessary link all the way around the torus. The induced currents in three-dimensional passive conductors [29, 28] are very different to those in toroidally continuous ones, but one might expect the destabilising quasi-steady ferromagnetic force to be broadly unchanged for discrete versus continuous components. The question remains open, but ref [15] discusses the effects of tiling ferromagnetic material and ref [30] proposes a route towards the numerical modelling of 3D ferromagnetic structures.

A Application of boundary conditions in cylindrical model problem

A.1 Plasma wire

The boundary conditions at the wall-exterior interface r_e are

$$\text{Normal flux:} \quad C_m^{(p,e)} = C_m^{(p,w)} + D_m^{(p,w)}(r_e/r_i)^{2m} \quad (54)$$

$$\text{Tangential field:} \quad \tilde{\mu}C_m^{(p,e)} = C_m^{(p,w)} - D_m^{(p,w)}(r_e/r_i)^{2m}. \quad (55)$$

Eliminating $C_m^{(p,e)}$, we get

$$(\tilde{\mu} - 1)(r_i/r_e)^m C_m^{(p,w)} + (\tilde{\mu} + 1)(r_e/r_i)^m D_m^{(p,w)} = 0. \quad (56)$$

The boundary conditions at the interior-wall interface r_i are

$$\text{Normal flux:} \quad C_m^{(p,w)} + D_m^{(p,w)} - D_m^{(p,i)} = C_m^{(p,i)} \quad (57)$$

$$\text{Tangential field:} \quad C_m^{(p,w)} - D_m^{(p,w)} + \tilde{\mu}D_m^{(p,i)} = \tilde{\mu}C_m^{(p,i)}. \quad (58)$$

Equations (56)–(58) may be solved simultaneously, with $C_m^{(p,e)}$ then coming from (54):

$$\begin{pmatrix} D_m^{(p,i)} \\ C_m^{(p,w)} \\ D_m^{(p,w)} \\ C_m^{(p,e)} \end{pmatrix} = \left[\frac{\tilde{\mu} - 1}{\tilde{\mu} + 1} \left(\frac{r_i}{r_e} \right)^m - \frac{\tilde{\mu} + 1}{\tilde{\mu} - 1} \left(\frac{r_e}{r_i} \right)^m \right]^{-1} \begin{pmatrix} (r_i/r_e)^m - (r_e/r_i)^m \\ -2\tilde{\mu}(r_e/r_i)^m/(\tilde{\mu} - 1) \\ 2\tilde{\mu}(r_i/r_e)^m/(\tilde{\mu} + 1) \\ -4\tilde{\mu}(r_e/r_i)^m/(\tilde{\mu}^2 - 1) \end{pmatrix} C_m^{(p,i)}. \quad (59)$$

A.2 Divertor coils

The boundary conditions at the interior-wall interface r_i are

$$\text{Normal flux:} \quad D_m^{(c,i)} = C_m^{(c,w)} + D_m^{(c,w)} \quad (60)$$

$$\text{Tangential field:} \quad \tilde{\mu}D_m^{(c,i)} = -C_m^{(c,w)} + D_m^{(c,w)}. \quad (61)$$

Eliminating $D_m^{(c,i)}$, we get

$$(\tilde{\mu} + 1)C_m^{(c,w)} + (\tilde{\mu} - 1)D_m^{(c,w)} = 0. \quad (62)$$

The boundary conditions at the wall-exterior interface r_e are

$$\text{Normal flux:} \quad C_m^{(c,w)} + D_m^{(c,w)}(r_e/r_i)^{2m} - C_m^{(c,e)} = D_m^{(c,e)}(r_e/r_i)^{2m} \quad (63)$$

$$\text{Tangential field:} \quad -C_m^{(c,w)} + D_m^{(c,w)}(r_e/r_i)^{2m} + \tilde{\mu}C_m^{(c,e)} = \tilde{\mu}D_m^{(c,e)}(r_e/r_i)^{2m}. \quad (64)$$

Equations (62)–(64) may be solved simultaneously, with $D_m^{(c,i)}$ then coming from (60):

$$\begin{pmatrix} D_m^{(c,i)} \\ C_m^{(c,w)} \\ D_m^{(c,w)} \\ C_m^{(c,e)} \end{pmatrix} = \left[\frac{\tilde{\mu} - 1}{\tilde{\mu} + 1} \left(\frac{r_i}{r_e} \right)^m - \frac{\tilde{\mu} + 1}{\tilde{\mu} - 1} \left(\frac{r_e}{r_i} \right)^m \right]^{-1} \begin{pmatrix} -4\tilde{\mu}(r_i/r_e)^m/(\tilde{\mu}^2 - 1) \\ 2\tilde{\mu}(r_i/r_e)^m/(\tilde{\mu} + 1) \\ -2\tilde{\mu}(r_i/r_e)^m/(\tilde{\mu} - 1) \\ (r_i/r_e)^m - (r_e/r_i)^m \end{pmatrix} (r_e/r_i)^{2m} D_m^{(c,e)}. \quad (65)$$

A.3 Time-dependent field

The boundary conditions at the wall-exterior interface r_e are

$$\text{Normal flux:} \quad (r_i/r_e)c^{(e)} = I_1(y_e)c^{(w)} + K_1(y_e)d^{(w)} \quad (66)$$

$$\text{Tangential field:} \quad \tilde{\mu}(r_i/r_e)c^{(e)} = [-y_e I_0(y_e) + I_1(y_e)]c^{(w)} + [y_e K_0(y_e) + K_1(y_e)]d^{(w)}. \quad (67)$$

Eliminating $c^{(e)}$, we get

$$[y_e l_0(y_e) + (\tilde{\mu} - 1) l_1(y_e)] c^{(w)} + [-y_e K_0(y_e) + (\tilde{\mu} - 1) K_1(y_e)] d^{(w)} = 0. \quad (68)$$

The boundary conditions at the interior-wall interface r_i are

$$\text{Normal flux:} \quad l_1(y_i) c^{(w)} + K_1(y_i) d^{(w)} - d^{(i)} = c^{(i)} \quad (69)$$

$$\text{Tangential field:} \quad -y_i l_0(y_i) c^{(w)} + y_i K_0(y_i) d^{(w)} + (\tilde{\mu} + 1) d^{(i)} = (\tilde{\mu} - 1) c^{(i)}. \quad (70)$$

Equations (68)–(70) may be solved simultaneously for the coefficients $d^{(i)}$, $c^{(w)}$ and $d^{(w)}$, with $c^{(e)}$ then coming from (66); in particular, the internal coefficients are related by

$$\frac{d^{(i)}}{c^{(i)}} = \frac{\alpha_1^+ - \alpha_K^+}{\alpha_1^- - \alpha_K^-}, \quad \text{where} \quad \alpha_1^\pm = \frac{\pm y_i l_0(y_i) + (\tilde{\mu} \mp 1) l_1(y_i)}{y_e l_0(y_e) + (\tilde{\mu} - 1) l_1(y_e)} \quad (71)$$

and α_K^\pm is the same expression with $l_0 \rightarrow -K_0$ and $l_1 \rightarrow K_1$, with $y_{i,e} = r_{i,e} \sqrt{\mu_1 \sigma \gamma}$.

B Thin-wall limit of cylindrical problem: stabilising force

Within the wall itself, the flux function $\psi^{(w)}$ satisfies (15) and hence solutions of the form (17) obey the differential equation

$$\frac{d}{dr} \left(r \frac{d\hat{\psi}^{(w)}}{dr} \right) = \left(\mu_1 \sigma \gamma r + \frac{1}{r} \right) \hat{\psi}^{(w)}. \quad (72)$$

We now integrate this over the thickness of the wall, from $r = r_i = r_w - \delta_w/2$ to $r = r_e = r_w + \delta_w/2$. Assuming the wall is thin, such that the right-hand side of (72) is approximately constant across it and terms of order δ_w/r_w may be ignored, then this becomes

$$\left\langle \frac{d\hat{\psi}^{(w)}}{dr} \right\rangle \approx \frac{\delta_w}{r_w^2} (\mu_1 \sigma \gamma r_w^2 + 1) \hat{\psi}^{(w)}(r_w) \quad (73)$$

where the angled brackets represent the jump across the wall. This quantity is related to the vacuum solutions by the boundary conditions (4). Furthermore, the right-hand side of (73) simplifies if the skin depth is much less than the wall radius (such that $\delta_w \ll s \ll r_w$). Then we have

$$\left\langle \frac{d\hat{\psi}}{dr} \right\rangle \approx \mu_0 \sigma \gamma \delta_w \hat{\psi}(r_w) \quad (74)$$

where it is now understood $\hat{\psi}$ pertains to the vacuum flux function ($\hat{\psi}^{(i)}$ and $\hat{\psi}^{(e)}$), and the wall thickness has been taken to zero. Note how this expression is independent of the magnetic permeability of the wall. Using the vacuum solution of the form (18) the corresponding matching equation is

$$c^{(i)} - d^{(i)} \approx (\mu_0 \sigma \gamma \delta_w r_w + 1) c^{(e)} \quad (75)$$

and since continuity of flux for a thin wall demands $c^{(i)} + d^{(i)} \approx c^{(e)}$, the approximate solution has

$$d^{(i)} \approx - \left(1 + \frac{2}{\mu_0 \sigma \gamma \delta_w r_w} \right)^{-1} c^{(i)}. \quad (76)$$

C Application of boundary conditions in spherical model problem

C.1 Plasma wire

The boundary conditions at the wall-exterior interface r_e are

$$\text{Normal flux:} \quad C_\ell^{(p,e)} = C_\ell^{(p,w)} + (r_e/r_i)^{2\ell+1} D_\ell^{(p,w)} \quad (77)$$

$$\text{Tangential field:} \quad \tilde{\mu} \ell C_\ell^{(p,e)} = \ell C_\ell^{(p,w)} - (\ell + 1) (r_e/r_i)^{2\ell+1} D_\ell^{(p,w)}. \quad (78)$$

Eliminating $C_\ell^{(p,e)}$, we get

$$(\tilde{\mu} - 1) \ell C_\ell^{(p,w)} + (\tilde{\mu}\ell + \ell + 1) (r_e/r_i)^{2\ell+1} D_\ell^{(p,w)} = 0. \quad (79)$$

The boundary conditions at the interior-wall interface r_i are

$$\text{Normal flux:} \quad C_\ell^{(p,w)} + D_\ell^{(p,w)} - D_\ell^{(p,i)} = C_\ell^{(p,i)} \quad (80)$$

$$\text{Tangential field:} \quad \ell C_\ell^{(p,w)} - (\ell + 1) D_\ell^{(p,w)} + \tilde{\mu}(\ell + 1) D_\ell^{(p,i)} = \tilde{\mu} \ell C_\ell^{(p,i)}. \quad (81)$$

Equations (79)–(81) may be solved simultaneously, with $C_\ell^{(p,e)}$ then coming from (77). In particular, the internal coefficients are related by

$$\frac{D_\ell^{(p,i)}}{C_\ell^{(p,i)}} = \frac{1 - (r_e/r_i)^{2\ell+1}}{\frac{(\tilde{\mu}-1)(\ell+1)}{\tilde{\mu}\ell+\ell+1} - \frac{\tilde{\mu}\ell+\ell+\tilde{\mu}}{\ell(\tilde{\mu}-1)} (r_e/r_i)^{2\ell+1}}. \quad (82)$$

If the wall is geometrically thin, $\delta_w \ll r_i$, then

$$\frac{D_\ell^{(p,i)}}{C_\ell^{(p,i)}} \approx \frac{\ell(\tilde{\mu} - 1)(\tilde{\mu}\ell + \ell + 1) \delta_w}{(2\ell + 1)\tilde{\mu} r_i}. \quad (83)$$

C.2 External coil pair

The boundary conditions at the interior-wall interface r_i are

$$\text{Normal flux:} \quad D_\ell^{(c,i)} = C_\ell^{(c,w)} + D_\ell^{(c,w)} \quad (84)$$

$$\text{Tangential field:} \quad \tilde{\mu}(\ell + 1) D_\ell^{(c,i)} = -\ell C_\ell^{(c,w)} + (\ell + 1) D_\ell^{(c,w)}. \quad (85)$$

Eliminating $D_\ell^{(c,i)}$, we get

$$(\tilde{\mu}\ell + \ell + \tilde{\mu}) C_\ell^{(c,w)} + (\tilde{\mu} - 1) (\ell + 1) D_\ell^{(c,w)} = 0. \quad (86)$$

The boundary conditions at the wall-exterior interface r_e are

$$\text{Normal flux:} \quad C_\ell^{(c,w)} + (r_e/r_i)^{2\ell+1} D_\ell^{(c,w)} - C_\ell^{(c,e)} = (r_e/r_i)^{2\ell+1} D_\ell^{(c,e)} \quad (87)$$

$$\text{Tangential field:} \quad -\ell C_\ell^{(c,w)} + (\ell + 1) (r_e/r_i)^{2\ell+1} D_\ell^{(c,w)} + \tilde{\mu} \ell C_\ell^{(c,e)} = \tilde{\mu} (\ell + 1) (r_e/r_i)^{2\ell+1} D_\ell^{(c,e)}. \quad (88)$$

Equations (86)–(88) may be solved simultaneously, with $D_\ell^{(c,i)}$ then coming from (84); these internal coefficients are given explicitly by

$$\frac{D_\ell^{(c,i)}}{D_\ell^{(c,e)}} = \frac{\tilde{\mu}(2\ell + 1)^2 (r_e/r_i)^{2\ell+1}}{(\tilde{\mu}\ell + \ell + \tilde{\mu}) (\tilde{\mu}\ell + \ell + 1) (r_e/r_i)^{2\ell+1} - \ell(\ell + 1)(\tilde{\mu} - 1)^2}. \quad (89)$$

If the wall is geometrically thin, $\delta_w \ll r_i$, then

$$\frac{D_\ell^{(c,i)}}{D_\ell^{(c,e)}} \approx 1 - \frac{\ell(\ell + 1)(\tilde{\mu} - 1)^2 \delta_w}{(2\ell + 1)\tilde{\mu} r_i}. \quad (90)$$

C.3 Time-dependent field

The boundary conditions at the wall-exterior interface r_e are

$$\text{Normal flux:} \quad (r_i/r_e)^{\ell+1} c_\ell^{(e)} = i_\ell(y_e) c_\ell^{(w)} + k_\ell(y_e) d_\ell^{(w)} \quad (91)$$

$$\text{Tangential field:} \quad \tilde{\mu} (r_i/r_e)^{\ell+1} c_\ell^{(e)} = [\ell i_\ell(y_e) - y_e i_{\ell-1}(y_e)] c_\ell^{(w)} + [\ell k_\ell(y_e) + y_e k_{\ell-1}(y_e)] d_\ell^{(w)}. \quad (92)$$

Eliminating $c_\ell^{(e)}$, we get

$$[\ell(\tilde{\mu} - 1) i_\ell(y_e) + y_e i_{\ell-1}(y_e)] c_\ell^{(w)} + [\ell(\tilde{\mu} - 1) k_\ell(y_e) - y_e k_{\ell-1}(y_e)] d_\ell^{(w)} = 0. \quad (93)$$

The boundary conditions at the interior-wall interface r_i are

$$\text{Normal flux:} \quad \mathbf{i}_\ell(y_i)c_\ell^{(w)} + \mathbf{k}_\ell(y_i)d_\ell^{(w)} - d_\ell^{(i)} = c_\ell^{(i)} \quad (94)$$

$$\text{Tangential field:} \quad -y_i\mathbf{i}_{\ell-1}(y_i)c_\ell^{(w)} + y_i\mathbf{k}_{\ell-1}(y_i)d_\ell^{(w)} + (\tilde{\mu}\ell + \ell + \tilde{\mu})d_\ell^{(i)} = \ell(\tilde{\mu} - 1)c_\ell^{(i)}. \quad (95)$$

Equations (93)–(95) may be solved simultaneously for the coefficients $d_\ell^{(i)}$, $c_\ell^{(w)}$ and $d_\ell^{(w)}$, with $c_\ell^{(e)}$ then coming from (91); in particular, the internal coefficients are given by

$$\frac{d_\ell^{(i)}}{c_\ell^{(i)}} = -\frac{\alpha_i^+ - \alpha_k^+}{\alpha_i^- - \alpha_k^-} \quad (96)$$

where

$$\alpha_i^\pm = \frac{[\tilde{\mu}(\pm\ell \pm \frac{1}{2} - \frac{1}{2}) - \ell] \mathbf{i}_\ell(y_i) + y_i\mathbf{i}_{\ell-1}(y_i)}{\ell(\tilde{\mu} - 1)\mathbf{i}_\ell(y_e) + y_e\mathbf{i}_{\ell-1}(y_e)} \quad (97)$$

and α_k^\pm is the same expression with $\mathbf{i}_\ell \rightarrow \mathbf{k}_\ell$ and $\mathbf{i}_{\ell-1} \rightarrow -\mathbf{k}_{\ell-1}$.

References

- [1] Steven J. Zinkle. Fusion materials science: Overview of challenges and recent progress. *Physics of Plasmas*, 12(5):058101, April 2005.
- [2] A. Kohyama, A. Hishinuma, D. S. Gelles, R. L. Klueh, W. Dietz, and K. Ehrlich. Low-activation ferritic and martensitic steels for fusion application. *Journal of Nuclear Materials*, 233-237:138–147, October 1996.
- [3] A Kohyama, A Hishinuma, Y Kohno, K Shiba, and A Sagara. The development of ferritic steels for DEMO blanket. *Fusion Engineering and Design*, 41(1):1–6, September 1998.
- [4] K. Mergia and N. Boukos. Structural, thermal, electrical and magnetic properties of Eurofer 97 steel. *Journal of Nuclear Materials*, 373(1-3):1–8, 2008.
- [5] K Ioki, V Barabash, A Cardella, F Elio, Y Gohar, G Janeschitz, G Johnson, G Kalinin, D Lousteau, M Onozuka, R Parker, G Sannazzaro, and R Tivey. Design and material selection for ITER first wall/blanket, divertor and vacuum vessel. *Journal of Nuclear Materials*, 258-263:74–84, October 1998.
- [6] A. Portone, M. Roccella, R. Roccella, F. Lucca, and G. Ramogida. The ITER TF coil ripple: Evaluation of ripple attenuation using Fe insert and of ripple enhancement produced by TBM. *Fusion Engineering and Design*, 83(10):1619–1624, December 2008.
- [7] D. A. Gates, J. Menard, R. Maingi, S. Kaye, S. A. Sabbagh, S. Diem, J. R. Wilson, M. G. Bell, R. E. Bell, J. Ferron, E. D. Fredrickson, C. E. Kessel, B. P. LeBlanc, F. Levinton, J. Manickam, D. Mueller, R. Raman, T. Stevenson, D. Stutman, G. Taylor, K. Tritz, and H. Yu. Progress towards steady state at low aspect ratio on the National Spherical Torus Experiment (NSTX). *Nuclear Fusion*, 47(9):1376–1382, September 2007.
- [8] D. Brunner, A. Q. Kuang, B. LaBombard, and J. L. Terry. The dependence of divertor power sharing on magnetic flux balance in near double-null configurations on Alcator C-Mod. *Nuclear Fusion*, 58(7):076010, May 2018.
- [9] C. Bachmann, W. Biel, S. Ciattaglia, G. Federici, F. Maviglia, G. Mazzone, G. Ramogida, F. Villone, and N. Taylor. Initial definition of structural load conditions in DEMO. *Fusion Engineering and Design*, 124:633–637, November 2017.
- [10] J. D. Jackson. *Classical Electrodynamics*. Wiley, New York, 3rd edition, 1999.
- [11] V. D. Pustovitov and V. V. Yanovskiy. Ferromagnetic effects in the theory of slow and fast resistive wall modes in tokamaks. *Physics of Plasmas*, 21(2):022516, February 2014.
- [12] V. S. Mukhovatov and V. D. Shafranov. Plasma equilibrium in a Tokamak. *Nuclear Fusion*, 11(6):605–633, December 1971.
- [13] E. A. Lazarus, J. B. Lister, and G. H. Neilson. Control of the vertical instability in tokamaks. *Nuclear Fusion*, 30(1):111–141, January 1990.
- [14] J. P. Levesque, P. E. Hughes, J. Bialek, P. J. Byrne, M. E. Mauel, G. A. Navratil, Q. Peng, D. J. Rhodes, and C. C. Stoaffer. Active and passive kink mode studies in a tokamak with a movable ferromagnetic wall. *Physics of Plasmas*, 22(5):056102, April 2015.
- [15] P. E. Hughes, J. P. Levesque, and G. A. Navratil. Dynamics of MHD instabilities near a ferromagnetic wall. *Nuclear Fusion*, 58(12):126009, September 2018.

- [16] A. Kirk, G. F. Counsell, H. R. Wilson, J.-W. Ahn, R. Akers, E. R. Arends, J. Dowling, R. Martin, H. Meyer, M. Hole, M. Price, P. B. Snyder, D. Taylor, M. J. Walsh, Y. Yang, and the MAST team. ELM characteristics in MAST. *Plasma Physics and Controlled Fusion*, 46(3):551–572, February 2004.
- [17] K. Tsuzuki, H. Kimura, H. Kawashima, M. Sato, K. Kamiya, K. Shinohara, H. Ogawa, K. Hoshino, M. Bakhtiari, S. Kasai, K. Uehara, H. Sasao, Y. Kusama, N. Isei, Y. Miura, T. Ogawa, M. Yamamoto, T. Shibata, K. Kikuchi, K. Miyachi, T. Ito, H. Ajikawa, S. Nomura, H. Tsutsui, R. Shimada, T. Ido, Y. Hamada, N. Fukumoto, M. Nagata, T. Uyama, H. Niimi, S. Yatsu, N. Kayukawa, T. Hino, Y. Hirohata, Y. Nagashima, A. Ejiri, A. Amemiya, Y. Sadamoto, and A. Tsushima. High performance tokamak experiments with a ferritic steel wall on JFT-2M. *Nuclear Fusion*, 43(10):1288–1293, October 2003.
- [18] M. Mori, N. Suzuki, T. Shoji, I. Yanagisawa, T. Tani, and Y. Matsuzaki. Stability limit of feedback control of vertical plasma position in the JFT-2M tokamak. *Nuclear Fusion*, 27(5):725–734, May 1987.
- [19] John Wesson. *Tokamaks*. Oxford University Press, Oxford, 4th edition, October 2011.
- [20] M. P. Gryaznevich, T. G. Kilovataya, and V. N. Pyatov. Effect of a ferromagnet on the equilibrium of a tokamak plasma. *Soviet Journal of Plasma Physics*, 9(4):414–417, 1983.
- [21] E. R. Solano, G. H. Neilson, and L. L. Lao. Equilibrium and stability studies for an iron core tokamak with a poloidal divertor. *Nuclear Fusion*, 30(6):1107–1115, June 1990.
- [22] D. P. O’Brien, L. L. Lao, E. R. Solano, M. Garribba, T. S. Taylor, J. G. Cordey, and J. J. Ellis. Equilibrium analysis of iron core tokamaks using a full domain method. *Nuclear Fusion*, 32(8):1351–1360, August 1992.
- [23] W. Zwingmann. Equilibrium analysis of steady state tokamak discharges. *Nuclear Fusion*, 43(9):842–850, August 2003.
- [24] L. C. Appel and I. Lupelli. Equilibrium reconstruction in an iron core tokamak using a deterministic magnetisation model. *Computer Physics Communications*, 223:1–17, February 2018.
- [25] J. A. Leuer. Passive Vertical Stability in the Next Generation Tokamaks. *Fusion Technology*, 15:489–494, March 1989.
- [26] Dai-Kai Sze, Mark Tillack, and Laila El-Guebaly. Blanket system selection for the ARIES-ST. *Fusion Engineering and Design*, 48(3):371–378, September 2000.
- [27] J. E. Menard, T. Brown, L. El-Guebaly, M. Boyer, J. Canik, B. Colling, R. Raman, Z. Wang, Y. Zhai, P. Buxton, B. Covele, C. D’Angelo, A. Davis, S. Gerhardt, M. Gryaznevich, M. Harb, T. C. Hender, S. Kaye, D. Kingham, M. Kotschenreuther, S. Mahajan, R. Maingi, E. Marriott, E. T. Meier, L. Mynsberge, C. Neumeyer, M. Ono, J.-K. Park, S. A. Sabbagh, V. Soukhanovskii, P. Valanju, and R. Woolley. Fusion nuclear science facilities and pilot plants based on the spherical tokamak. *Nuclear Fusion*, 56(10):106023, August 2016.
- [28] V. D. Pustovitov. Disruption forces on the tokamak wall with and without poloidal currents. *Plasma Physics and Controlled Fusion*, 59(5):055008, March 2017.
- [29] P. H. Titus, S. Avasaralla, A. Brooks, and R. Hatcher. NSTX disruption simulations of detailed divertor and passive plate models by vector potential transfer from OPERA global analysis results. *Fusion Engineering and Design*, 86(9):1784–1790, October 2011.
- [30] L. Barbato, S. Mastrostefano, G. Rubinacci, S. Ventre, and F. Villone. Effect of 3D Ferromagnetic Materials on Plasma Nonlinear Evolution in Fusion Devices. In *42nd EPS Conference on Plasma Physics*, Lisbon, 2015.